AGU PUBLICATIONS

JGR

Journal of Geophysical Research: Oceans

RESEARCH ARTICLE

10.1002/2016JC011899

Key Points:
- Synoptic-to-planetary scale wind variability enhances phytoplankton at ocean fronts due to enhanced mixing and upwelling of nutrients
- Wind-driven mixing layers are more variable, reach deeper maximum depths, and drive greater nutrient entrainment at fronts
- Oscillatory along-front winds spin down fronts and drive a time-mean upwelling of nutrient, which enhances subsurface phytoplankton

Supporting Information:
- Supporting Information S1

Correspondence to:
D. B. Whitt,
dan.whitt@gmail.com

Citation:
Whitt, D. B., J. R. Taylor, and M. Lévy (2017), Synoptic-to-planetary scale wind variability enhances phytoplankton biomass at ocean fronts, *J. Geophys. Res. Oceans*, *122*, 4602–4633, doi:10.1002/2016JC011899.

Received 18 APR 2016
Accepted 5 MAY 2017
Accepted article online 15 MAY 2017
Published online 3 JUN 2017

Synoptic-to-planetary scale wind variability enhances phytoplankton biomass at ocean fronts

D. B. Whitt[1,2], J. R. Taylor[1], and M. Lévy[3]

[1]Department of Applied Mathematics and Theoretical Physics, Centre for Mathematical Sciences, University of Cambridge, Cambridge, UK, [2]Climate and Global Dynamics Division, National Center for Atmospheric Research, Boulder, Colorado, USA, [3]Sorbonne Universités (UPMC, Univ Paris 06)-CNRS-IRD-MNHN, LOCEAN, IPSL, Paris, France

Abstract In nutrient-limited conditions, phytoplankton growth at fronts is enhanced by winds, which drive upward nutrient fluxes via enhanced turbulent mixing and upwelling. Hence, depth-integrated phytoplankton biomass can be 10 times greater at isolated fronts. Using theory and two-dimensional simulations with a coupled physical-biogeochemical ocean model, this paper builds conceptual understanding of the physical processes driving upward nutrient fluxes at fronts forced by unsteady winds with timescales of 4–16 days. The largest vertical nutrient fluxes occur when the surface mixing layer penetrates the nutricline, which fuels phytoplankton in the mixed layer. At a front, mixed layer deepening depends on the magnitude and direction of the wind stress, cross-front variations in buoyancy and velocity at the surface, and potential vorticity at the base of the mixed layer, which itself depends on past wind events. Consequently, mixing layers are deeper and more intermittent in time at fronts than outside fronts. Moreover, mixing can decouple in time from the wind stress, even without other sources of physical variability. Wind-driven upwelling also enhances depth-integrated phytoplankton biomass at fronts; when the mixed layer remains shallower than the nutricline, this results in enhanced subsurface phytoplankton. Oscillatory along-front winds induce both oscillatory and mean upwelling. The mean effect of oscillatory vertical motion is to transiently increase subsurface phytoplankton over days to weeks, whereas slower mean upwelling sustains this increase over weeks to months. Taken together, these results emphasize that wind-driven phytoplankton growth is both spatially and temporally intermittent and depends on a diverse combination of physical processes.

1. Introduction

Observations reveal significant spatiotemporal variability in phytoplankton chlorophyll at the ocean mesoscale (10–100 km, days to weeks) [e.g., *Gower et al*., 1980; *Denman and Abbott*, 1994] and submesoscale (0.1–10 km, hours to days) [e.g., *Strass*, 1992; *Yoder et al*., 1993; *Washburn et al*., 1998; *Thyssen et al*., 2009; *van Gennip et al*., 2016; *Moses et al*., 2016]. However, the phytoplankton variability at these scales is driven by coupled physical, biogeochemical, and ecosystem dynamics that are mostly unresolved in global coupled ocean-biogeochemistry models, difficult to observe, and poorly understood.

In some circumstances, frontal dynamics may significantly modify phytoplankton biomass distributions and growth rates at the mesoscale and submesoscale [e.g., *Woods*, 1988; *Strass*, 1992; *Lévy et al*., 2001; *Lévy and Klein*, 2004; *Klein and Lapeyre*, 2009; *McGillicuddy*, 2016; *Mahadevan*, 2016]. Mesoscale and submesoscale fronts are ubiquitous [e.g., *Mied et al*., 1986; *Pollard and Regier*, 1992; *Orsi et al*., 1995; *Rudnick and Luyten*, 1996; *Nagai et al*., 2009; *Belkin et al*., 2009; *Inoue et al*., 2010; *Li et al*., 2012], and observations show that fronts are associated with anomalous biogeochemical properties relative to the waters on either side. In particular, fronts are associated with elevated nutrients and stronger upward nutrient fluxes [e.g., *Allen et al*., 2005; *Li et al*., 2012], higher primary productivity [e.g., *Fernández and Pingree*, 1996], more chlorophyll and depth-integrated biomass [e.g., *Claustre et al*., 1994; *Granata et al*., 1995; *Fernández and Pingree*, 1996; *Niewiadomska et al*., 2008; *Davis et al*., 2008; *Li et al*., 2012], different plankton communities [e.g., *Claustre et al*., 1994; *Taylor et al*., 2012; *Krause et al*., 2015], and larger organic carbon export fluxes [e.g., *Omand et al*., 2015; *Stukel et al*., 2017]. Moreover, numerical simulations suggest several reasons why fronts are associated with anomalous biogeochemistry. For example, in regions where phytoplankton growth is limited by low nutrient concentrations, phytoplankton growth is enhanced at fronts, where the nutrient transport to the euphotic zone is enhanced due to: (1) upwelling driven by meandering and frontogenesis [e.g., *Woods*, 1988;

Mahadevan and Archer, 2000; *Lévy et al*., 2001; *Martin et al*., 2001; *Lima et al*., 2002; *Klein and Lapeyre*, 2009], (2) upwelling in wind-driven vertical circulations [e.g., *Franks and Walstad*, 1997; *Nagai et al*., 2008; *Mahadevan et al*., 2008; *Lévy et al*., 2009], (3) upwelling in symmetric instability (SI) cells [e.g., *Brannigan*, 2016], and (4) nutrient entrainment into deeper surface mixing layers (SXLs) [e.g., *Lévy et al*., 2009; *Whitt et al*., 2017]. However, the global significance of frontal physics for biogeochemistry is still a subject of ongoing study because fronts are difficult to resolve in global ocean-biogeochemistry simulations and difficult to observe in the ocean [e.g., *Oschlies*, 2002; *McGillicuddy et al*., 2003; *Ferrari*, 2011; *Lévy et al*., 2012a,2012b; *McGillicuddy*, 2016; *Mahadevan*, 2016].

Moreover, the conceptual models of the physical processes driving biogeochemical dynamics at fronts are incomplete. For example, although it is well-known that wind can modify biogeochemistry at a front by enhancing vertical mixing and vertical advection at the front, it is not known how the different timescales associated with unsteady wind [see e.g., *Gille*, 2005] impact vertical nutrient transport and biogeochemistry at a front. *Lévy et al*. [2009] and *Whitt et al*. [2017] suggest that high-frequency near-inertial wind variance (at periods ranging from about 0.5–2 days), which generates inertial oscillations in the ocean mixed layer, significantly enhances vertical transport of nutrient and hence phytoplankton growth at fronts. This paper takes another step toward a more complete conceptual understanding of how wind-stress variability impacts biogeochemistry at fronts by exploring how lower-frequency synoptic-to-planetary scale wind variance (at periods ranging from 4 to 16 days) impacts vertical nutrient transport and phytoplankton biomass at fronts in nutrient-limited open-ocean conditions in the midlatitudes (this context will be assumed hereafter).

The analysis is conducted using output from numerical simulations of idealized fronts in a two-dimensional (2-D) coupled physical-biogeochemical ocean model configuration similar to *Franks and Walstad* [1997] and forced by different wind scenarios; the simulation setup is described in section 2. In order to highlight the effects of the time-dependent winds, several potentially relevant physical processes are excluded from the simulations presented here, including frontal meandering [unlike *Woods*, 1988; *Lévy et al*., 2001], three-dimensional mixed-layer baroclinic instabilities [unlike *Mahadevan et al*., 2012; *Taylor*, 2016], spatial variations in the wind stress on the horizontal scale of the ocean fronts [unlike *Martin and Richards*, 2001; *McGillicuddy et al*., 2007], and explicit influences from larger-scale oceanic processes. In addition, only modest wind stress magnitudes $|\tau| < 0.25$ N/m^2 (wind speeds less than about 12.5 m/s at 10 m height) are considered; the effects of very intense storms are not considered.

This paper makes three main contributions to the literature on physical-biogeochemical interaction at ocean fronts. First, section 3 characterizes the nutrient transport and phytoplankton biomass response at a front forced by a transient (i.e., 8 day long) along-front wind stress with a constant magnitude. Although the physics that modifies nutrient transport and phytoplankton biomass at a front forced by a transient constant wind stress has been discussed previously [e.g., *Franks and Walstad*, 1997; *Thomas*, 2005; *Mahadevan et al*., 2008; *Nagai et al*., 2008; *Brannigan*, 2016], novel insights are derived from a new physical theory, which encapsulates the primary physical processes that modify phytoplankton biomass at a front forced by a transient constant wind stress in a single differential equation. The second main contribution, in section 4, is a characterization of the nutrient transport and phytoplankton biomass response at a front forced by oscillatory low-frequency wind (with 4–16 day periods characteristic of synoptic-to-planetary scale atmospheric variability). These simulation results reveal two physical hysteresis effects that modify biogeochemistry under oscillatory wind, are absent in the simulation forced by a transient constant wind and, as far as we know, have not been noted in a previous publication. The third main contribution, in section 5, is a characterization of the nutrient transport and phytoplankton biomass response at a front forced by a realistic wind. Although it is beyond the scope of this article to fully explore how phytoplankton respond to unsteady wind over a front, the simulation forced by the realistic wind provides some insight into: (1) how phytoplankton biomass might respond to unsteady wind at a front under a more realistic wind forcing, and (2) the robustness of the conclusions derived from more idealized simulations.

2. Simulation Setup

This paper's interpretation of the biogeochemical response to wind at a front is based primarily on simulations with a 2-D coupled physical-biogeochemical ocean model. The first three sections below describe the

2-D model, including (2.1) the physical model and initial conditions, (2.2) the biogeochemical model and initial conditions, and (2.3) the wind forcing scenarios. Section 2.4 describes a 1-D version of the physical-biogeochemical model that is used to help interpret the 2-D simulations.

2.1. Two-Dimensional Physical Model and Initial Condition

The 2-D physical model is based on the incompressible hydrostatic primitive equations on a midlatitude f-plane ($f=10^{-4}$ s^{-1}) with the Boussinesq approximation and only one dynamical tracer, that is density ρ or equivalently buoyancy $b=-g\rho/\rho_0$, where $\rho_0=1027$ kg/m^3 is the reference density of seawater and $g=9.81$ m/s^2 is the acceleration due to gravity. Only low-aspect-ratio hydrostatic motions are explicitly resolved in the simulations; nonhydrostatic processes such as convection, Kelvin-Helmholtz type shear instabilities, mixing by high-frequency internal wave breaking, and three-dimensional turbulence are parameterized by the K-profile-parameterization (KPP) scheme [e.g., *Large et al*., 1994]. The analysis will refer at various points to the surface boundary layer (SBL), which is defined as in *Large et al*. [1994] (see (1) in the supporting information) and represents the depth of the surface layer of high vertical diffusivity and viscosity. The SBL is to be compared with the surface mixing layer (SXL), a term which is used in this paper to loosely describe the dynamically active layer encompassing strong wind-driven vertical tracer and momentum fluxes due to both resolved and parameterized processes. The SXL and the SBL are in many cases nearly identical, but sometimes differ in the simulations presented in this paper due to low-aspect-ratio SI with horizontal wavelengths $\sim$1 km [e.g., *Thomas*, 2005; *Taylor and Ferrari*, 2010], which is partially resolved here [*Bachman and Taylor*, 2014] and sometimes extends below the SBL. The explicit horizontal viscosity $\nu_h=1$ m^2/s is constant and crudely represents the horizontal mixing of momentum by small-scale internal waves and vortical motions that are not resolved. The explicit horizontal diffusivity $K_h=0$ m^2/s in order to isolate the effects of tracer transport by resolved advection and parameterized vertical mixing. The chosen computational grid has a uniform horizontal grid spacing of $\Delta y=300$ m and a stretched vertical grid spacing with higher resolution near the surface ($\Delta z\approx 2$ m at $z=-100$ m depth). The resolution is sufficiently fine that halving the grid spacing in both the horizontal and vertical directions (e.g., in the simulation labeled DR for double resolution in Table 1) does not significantly change the results (see supporting information Figure S10). Additional details of the numerical implementation in the Regional Ocean Modeling System (ROMS) appear in supporting information section S2 [*Shchepetkin and McWilliams*, 2005; *Smolarkiewicz and Margolin*, 1998; *Large et al*., 1994].

Table 1. List of All the Forcing Scenarios Associated With 2-D Simulations in This Paper[a]

Label	Surface Stress Function	Mixing	Grid ($y\times z$)	Orient
1. NF	0	KPP	400 × 200	n/a
2. XW	$.18\cos(.09ft)$	KPP	400 × 200	Along-front
3. YW	$.18\cos(.09ft)$	KPP	400 × 200	Across-front
4. VM	0	$K_z(y,z)=\bar{K}^t_z(y,z)$ in XW	400 × 200	n/a
5. VMT	0	$K_z(y,z,t)$ as in XW	400 × 200	n/a
6. CM	$.18\cos(.09ft)$	$K_z=2\times10^{-5}$	400 × 200	Along-front
7. CW	0.06	KPP	400 × 200	Along-front
8. RW	From buoy data	KPP	400 × 200	Variable
9. XW.06	$.06\cos(.09ft)$	KPP	400 × 200	Along-front
10. XW.12	$.12\cos(.09ft)$	KPP	400 × 200	Along-front
11. XW.24	$.24\cos(.09ft)$	KPP	400 × 200	Along-front
12. XW 4d	$.12\cos(.18ft)$	KPP	400 × 200	Along-front
13. XW 16d	$.12\cos(.045ft)$	KPP	400 × 200	Along-front
14. XW DR	$.18\cos(.09ft)$	KPP	800 × 400	Along-front

[a]The surface stress is in N/m^2 and the vertical diffusivity K_z is in m^2/s. The mixing column indicates the vertical mixing scheme. KPP means that the vertical diffusivity applied to biogeochemical variables varies in time and space and is equal to the vertical diffusivity of density determined by the KPP scheme, whereas CM (constant biogeochemical mixing) indicates that the vertical mixing coefficients applied to biogeochemical variables are constant and momentum/density mixing is determined by KPP. VM (variable mixing) indicates that the vertical mixing coefficients applied to all variables are fixed as a spatially variable input, whereas VMT (time-variable vertical mixing) indicates that the vertical mixing coefficients applied to all variables are imposed as spatially and temporally variable inputs. The input mixing coefficients are chosen to match the 75 day time mean (VM) and the 3 h-average output from the XW simulation (VMT). All the idealized wind stresses are oriented along the front in X (i.e., they are x-winds) except YW, which is oriented in the cross-front direction (i.e., as y-winds). In the realistic wind scenario (RW), the wind magnitude and direction vary with time as described in section 5.

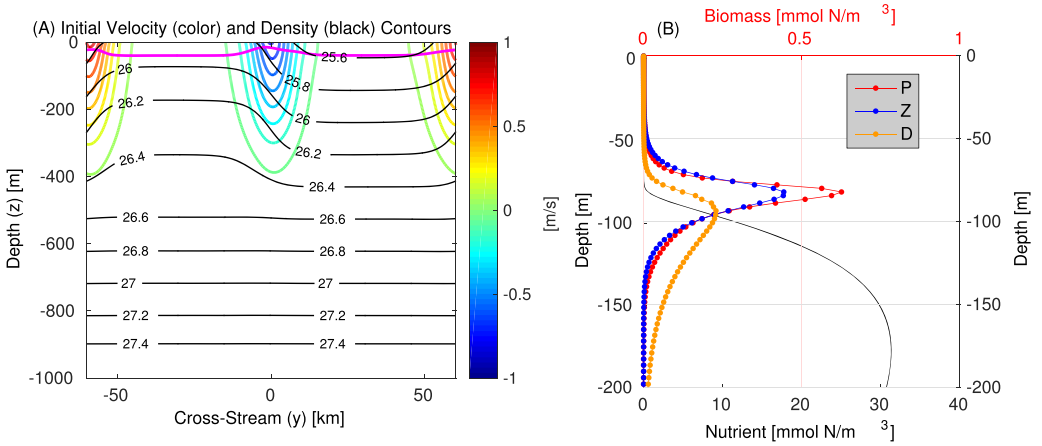

Figure 1. The initial conditions for (a) the physical model and (b) the biogeochemical model. The velocity field (color) is in thermal wind balance with the density field (thin black lines every 0.2 kg/m^3), and a free surface displacement (not shown) cancels the baroclinic pressure gradient leading to a level of no motion at the bottom. The surface density difference across the front is about.35 kg/m^3 and the background $\partial b/\partial z = 2\times10^{-5}$ s^{-2}. The initial phytoplankton, zooplankton, detritus, and nutrient (P, Z, D, and N) are horizontally uniform and are initially in a sinking-diffusion equilibrium. The high-diffusivity SBL depth H_{sbl}, which is defined by KPP, after 3 h of forcing by a stress $\tau_x =$ 0.18 N/m^2 is shown in magenta in Figure 1a.

The physical initial condition is constructed, as described in supporting information section S3, to represent an open-ocean region without boundaries or variable bathymetry and with isolated geostrophic fronts with characteristics that are intermediate between the mesoscale and submesoscale. The initial density and velocity fields for all the simulations are shown in Figure 1a. The domain contains a pair of isolated surface-intensified geostrophic fronts superimposed on a background stratification $\partial b/\partial z = 2\times10^{-5}$ s^{-2}. The domain is periodic in the cross-front direction and bounded by a flat bottom at $z = -1000$ m and a free surface at $z = 0$ m. Since fronts are anisotropic features with much stronger vertical and cross-front gradients than along-front gradients [e.g., *Fedorov*, 1986], the simulated fronts have strong vertical (z) and cross-front (y) gradients and zero along-front (x) gradient. That is, all three components of the velocity vector are retained, but all resolved processes are uniform in the along-front direction ($\partial/\partial x = 0$).

This paper builds a conceptual understanding of the physical and biogeochemical response to unsteady winds at a geostrophic front with physical characteristics that are broadly representative of observed fronts. In particular, the simulations are not designed to represent any particular ocean, or any particular time of year, or any particular front. However, it may be noted that the peak velocity and horizontal scale of the frontal jets in Figure 1a are qualitatively similar to the frontal jets observed by *Mied et al.* [1986] and *Pollard and Regier* [1992] in the Sargasso Sea, by *Claustre et al.* [1994] in the East Alboran Sea, and in the California Current System by *Li et al.* [2012]. On the other hand, the velocity magnitudes, velocity gradients, and horizontal and vertical frontal length scales are smaller than those observed in the Kuroshio [e.g., *Nagai et al.*, 2009] and the Gulf Stream [e.g., *Inoue et al.*, 2010]. Further discussion of oceanic context of the physical initial condition is presented in supporting information section S3 in terms of nondimensional physical parameters [*Hoskins*, 1974; *Gill*, 1982; *Thomas et al.*, 2008; *McWilliams*, 2016]. Although the sensitivity of the results to the physical parameters of the initial condition is not explicitly explored with 2-D sensitivity simulations here, theoretical arguments, which are developed throughout the paper, provide insight into how the biogeochemical response depends on the physical parameters that characterize the front.

2.2. Biogeochemical Model and Initial Conditions

The physical model is coupled to a four-component nutrient, phytoplankton, zooplankton, and detritus (NPZD) biogeochemical model [e.g., *Fasham et al.*, 1990]. The biogeochemical model equations, which appear in supporting information section S4, are slightly modified from those of *Powell et al.* [2006], which are implemented in the publicly available version of ROMS. The model parameters, which are presented in supporting information Table S1, differ significantly from those of *Powell et al.* [2006] so that the biogeochemical equilibrium in a 1-D column with a modest background vertical diffusivity $K_z = 2\times10^{-5}$ m^2/s (i.e., Figure 1b) is crudely representative of an idealized nutrient-limited open ocean in the midlatitudes. Yet, the

biogeochemical model is not tuned to represent any specific ocean at any specific time of year, and the qualitative results may apply anywhere deep nutrients limit phytoplankton growth in the euphotic zone.

The biogeochemical initial condition for the 2-D model consists of the horizontally uniform profiles in Figure 1b and is characterized by an equilibrium (i.e., steady state) subsurface phytoplankton maximum (SPM). This initial condition for the 2-D model is obtained from a 10 year simulation with only a constant vertical diffusivity $K_z = 2\times10^{-5}$ m^2/s driving vertical fluxes of the biogeochemical constituents in a 1-D column on the same stretched vertical grid as the 2-D model and initial $N = 14$ mmol N/m^3 and $P, Z, D = 2$ mmol N/m^3. An interpretation of this equilibrium in the initial condition, which manifests as a balance primarily between sinking detritus and upward diffusion of nutrient, was given by *Riley et al*. [1949], but see also the recent review by *Cullen* [2015] and the references therein. Although a SPM appears with a wide range of NPZD model parameters and in many different oceanic regimes, the detailed structure, such as the depth, thickness, and magnitude of the maximum phytoplankton concentration in the SPM are controlled by the modeling choices made here [e.g., *Beckmann and Hense*, 2007]. The biogeochemical model parameters are chosen so that the SPM depth is within the range of observed SPM depths. An explicit description of how variations in the model parameters modify the initial profile and the SPM is included in supporting information section S4.1 [*Franks et al*., 1986; *Steele and Henderson*, 1992; *Edwards and Brindley*, 1999; *Edwards and Yool*, 2000]. Although the sensitivity of the results to the biogeochemical model and model parameters is not explicitly addressed with 2-D sensitivity simulations here, a discussion of how the biogeochemical response to wind forcing depends on the depth of the initial SPM and hence the biogeochemical model parameters is in section 3.2 below.

2.3. Forcing the Two-Dimensional Model

Unless otherwise stated, the wind stresses are specified as spatially uniform surface stress boundary conditions with the different time-dependent forms given in Table 1, the vertical mixing coefficients are set internally by KPP for density and momentum, and biogeochemical variables are mixed with the same vertical diffusivity as density. However, in some cases (e.g., CM, VM, and VMT in Table 1) the vertical viscosity ν_z and/or diffusivity K_z are specified externally via input, rather than internally via KPP. All other model parameters—with the exception of the surface stress and the vertical mixing scheme—are the same in all 2-D simulations in order to isolate the effects of the wind. Table 1 contains a list of the forcing functions and mixing schemes for all the 2-D simulations that are discussed in this paper.

2.4. One-Dimensional Model

Oscillatory winds naturally induce a mostly oscillatory physical response, and the time mean physical response to the oscillatory forcing emerges only as a smaller residual. Some important questions arise in this context: what are the average biogeochemical effects of purely oscillatory vertical transport [e.g., *Holloway*, 1984]? How do the time-integrated biogeochemical effects due to the purely oscillatory vertical transport compare with the time-integrated biogeochemical effects due to the time-mean or forcing-period-averaged vertical transport in a front? These questions are addressed in section 4 with the aid of a 1-D advection-diffusion physical model coupled to the same biogeochemical model used in the 2-D simulations.

The 1-D model is implemented in Matlab [see *Whitt*, 2017a], as described in supporting information section S5, in order to facilitate rapid exploration of the biogeochemical response to different combinations of oscillatory and mean vertical motions, different vertical diffusivities, and different biogeochemical parameters. Although the 1-D model grid and numerical differentiation are not identical to those of the 2-D model, the number of grid points in the 1-D model is sufficiently large and the domain sufficiently deep that the 1-D simulation results are effectively unchanged if the grid spacing is doubled and the domain depth is doubled (supporting information Figures S1 and S2). Hence, the numerical implementation of the 1-D model should not have any significant implication for the results.

The biogeochemical fields in the 1-D model are advected by imposed vertically uniform vertical velocity time series $w(t)$, which are derived from time series of Lagrangian drifter displacements obtained from the online advection of an array of 38 virtual Lagrangian drifters in the 2-D simulations. The drifters are initially evenly spaced from $y = -12.5$ to $+12.5$ km at $z = -105$ m (below the SXL) and advected forward in time online during a 2-D simulation by the full velocity field using a fourth-order Milne predictor [*Abramowitz*

and Stegun, 1964] and a fourth-order Hamming corrector scheme [*Hamming*, 1973]. The drifter positions are saved every hour; supporting information Figure S4 shows the drifter trajectories in the XW simulation (see Table 1) before any additional postprocessing. This Lagrangian approach is used to define the Eulerian vertical velocity in the 1-D model because the Eulerian mean vertical velocity derived from the 2-D model can—in some circumstances—misrepresent the mean vertical circulation that drives tracer fluxes in a flow dominated by perturbations, for example when the generalized Stokes drift is significant [e.g., *Andrews and McIntyre*, 1978; *Plumb*, 1979].

The postprocessing steps to construct the vertical velocities for input into the 1-D model are as follows: first, the array of 38 drifters is used to obtain 25 time series of Lagrangian vertical displacement $\zeta(y_i,t)$, one for each cross-front kilometer from $y_1=-12$ km to $y_{25}=+12$ km. Each $\zeta(y_i,t)$ represents the average vertical displacement of the group of drifters that are *initially* within ±500 m of y_i (one or two drifters per group). Then, the $\zeta(y_i,t)$ is time-filtered with a 48 h moving average to eliminate high-frequency inertia-gravity waves (which are nonnegligible at the beginning of the simulations) and retain the low-frequency Ekman suction. Third, a discrete time derivative is applied to obtain the vertical velocity $w(y_i,t)=d\zeta(y_i,t)/dt$. Fourth, the Lagrangian mean vertical velocity $\langle w\rangle(y_i)$ is calculated at each y_i, where $\langle w\rangle(y_i)=\frac{1}{T}\int_0^T w(y_i,t)dt$ with $T\approx72$ days or nine forcing periods, and the perturbation vertical velocity is calculated as $w(y_i,t)-\langle w\rangle(y_i)$.

Then, for a given 2-D simulation, three sets of 25 1-D simulations are executed: in one set the vertical advection is by the full vertical velocity $w(t)$, in a second set the vertical advection is by the time-mean vertical velocity $\langle w\rangle$, and in a third set the vertical advection is by the perturbation vertical velocity $w(t)-\langle w\rangle$. In all cases presented here, the vertical diffusivity in the 1-D simulations is set to a background constant $K_z=2\times10^{-5}$ m^2/s. Each 1-D simulation represents a 1 km wide region (in y) of the primary 2-D simulation where the relevant drifters were initialized.

3. Transient Constant Wind

This section analyses the transient physical and biogeochemical response to a wind with a constant stress at a modest amplitude $\tau_x=0.06$ N/m^2 (equivalent to a wind speed of about 6 m/s at 10 m height) maintained for 8 days; this wind scenario is referred to as the constant wind (CW) scenario in Table 1. Although the wind stress is always unsteady in the real ocean, several previous model-based process studies of biogeochemistry at fronts have focused on the biogeochemical response to transient periods of constant wind stress [e.g., *Franks and Walstad*, 1997; *Nagai et al*., 2008; *Mahadevan et al*., 2008]. To our knowledge, no previous study has explicitly explored the biogeochemical response to a purely oscillatory (i.e., zero time mean) wind at a front (except the companion study *Whitt et al*. [2017]) (but see *Mahadevan et al*. [2010]; *Siedlecki et al*., [2011, 2012]). Hence, the results of this paper begin with an analysis of the simpler and more familiar CW simulation before analyzing simulations with oscillatory wind forcing. This CW simulation and the associated analysis serve as a point of reference, to which the simulations forced by oscillatory and realistic wind can be compared.

3.1. Description of the CW Simulation

The magnitude of the wind stress in the CW simulation is not sufficiently strong to drive SXLs deep enough to modify the nutrient N or phytoplankton P concentration distributions outside the front. Hence, the vertical profiles of N and P remain essentially unchanged outside the front throughout the 8 day simulation. However, the wind induces N and P anomalies at the fronts by driving vertical velocities at the nutricline and by driving entrainment of nutrient into deep SXLs, which vary across the fronts and reach their deepest depths on the less dense side of the front centered at $y=\pm60$ km (Figures 2 and 3).

At both fronts, the vertical displacements of the nutricline and the associated N anomalies below the SXL exhibit a tripolar structure (Figures 2e and 2f), which is characteristic of vertical advection by Ekman suction [e.g., *Stern*, 1965; *Niiler*, 1969; *Stern*, 1975; *Lee et al*., 1994],

$$w_{Ek}=\frac{\partial M_{Ek}}{\partial y}, \tag{1}$$

where the generalized cross-front Ekman transport

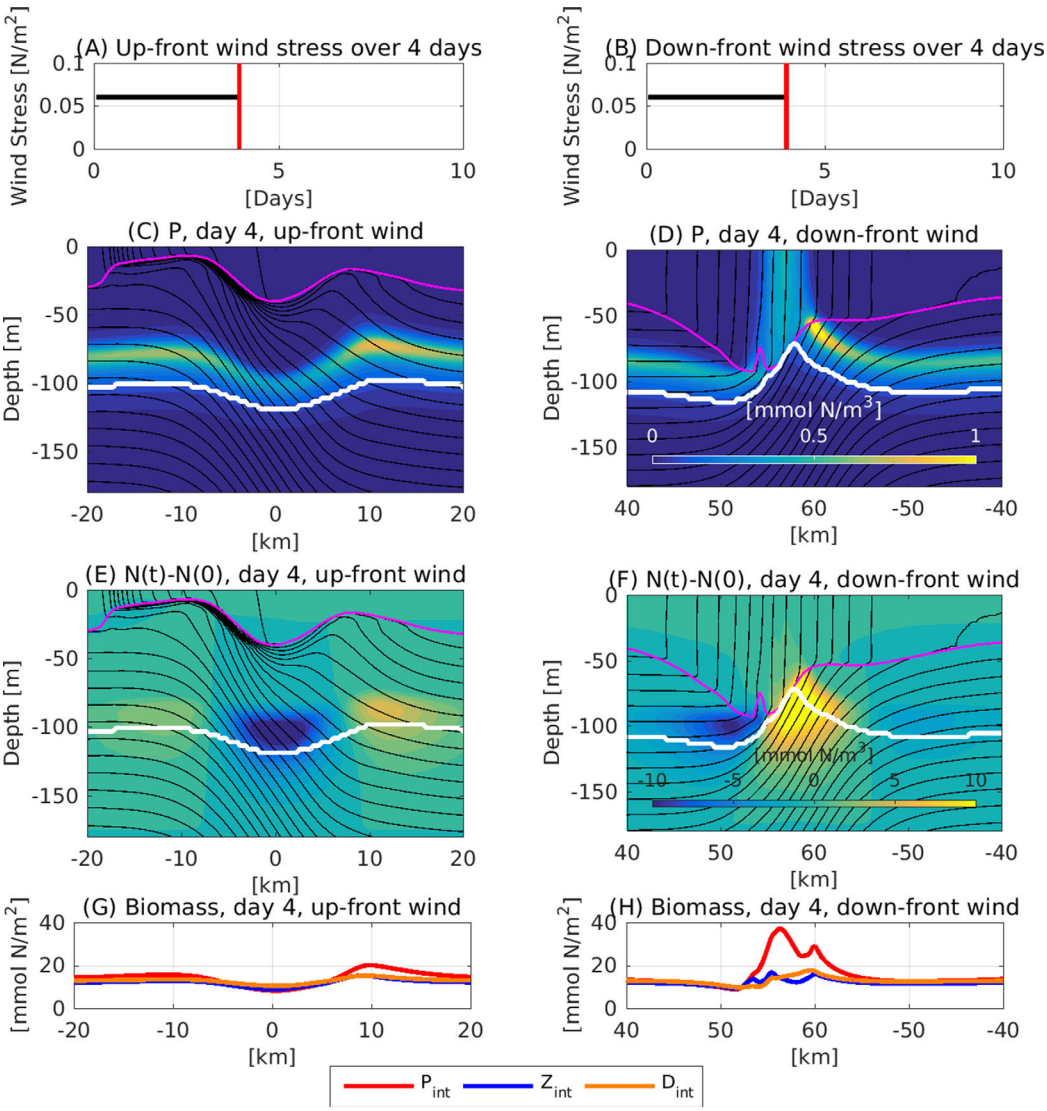

Figure 2. Snapshots of the biogeochemistry on day 4 in the CW scenario. (left) The front centered at $y = 0$ km, where the wind points up-front, and (right) the front centered at $y = \pm 60$ km, where the wind points down-front. (a and b) Wind stress time series, (c and d) phytoplankton concentration P, and (e and f) nutrient concentration anomaly, i.e., $N(t = 4\ \mathrm{d}) - N(0)$. Overlaid in Figures 2c–2f are density contours every.025 kg/m^3 in black, the depth of the $N = 15$ mmol/m^3 nutrient isopleth $H_{N=15}$ in white, and the high-diffusivity SBL depth H_{sbl} in magenta. (g and h) Full-depth-integrated phytoplankton P_{int} in red, zooplankton Z_{int} in blue, and detritus D_{int} in orange.

$$M_{Ek} = -\frac{\tau_x}{\rho\left(f - \frac{\partial u}{\partial y}\right)}. \tag{2}$$

Even when the along-front stress does not vary across the front, as in all the simulations presented in this paper, M_{Ek} varies across the front due to variations in the absolute vertical vorticity $f - \partial u/\partial y$ at the surface, which is between $0.3f$ and $1.7f$ at the start of the simulations. The divergence of the Ekman transport drives Ekman suction. When the wind is down-front (i.e., in the same direction as the geostrophic frontal jet centered at $y = \pm 60$ km), the nutricline rises near the middle of the front and descends near the flanks (near $y = \pm 50$ km, see Figure 2f). When the wind is up-front (i.e., opposite to the geostrophic jet centered at $y = 0$ km), the nutricline descends near the middle of the front and rises near the flanks (near $y = \pm 10$ km, see Figure 2e). After 4 days, the locations where the nutricline has risen are associated with positive anomalies in N and P at the SPM and increased depth-integrated phytoplankton biomass $P_{int} = \int_{z=-1000}^{0} P dz$, whereas the locations where the nutricline has descended are associated with negative anomalies in N and P at the SPM and reduced P_{int} (Figures 2c–2h).

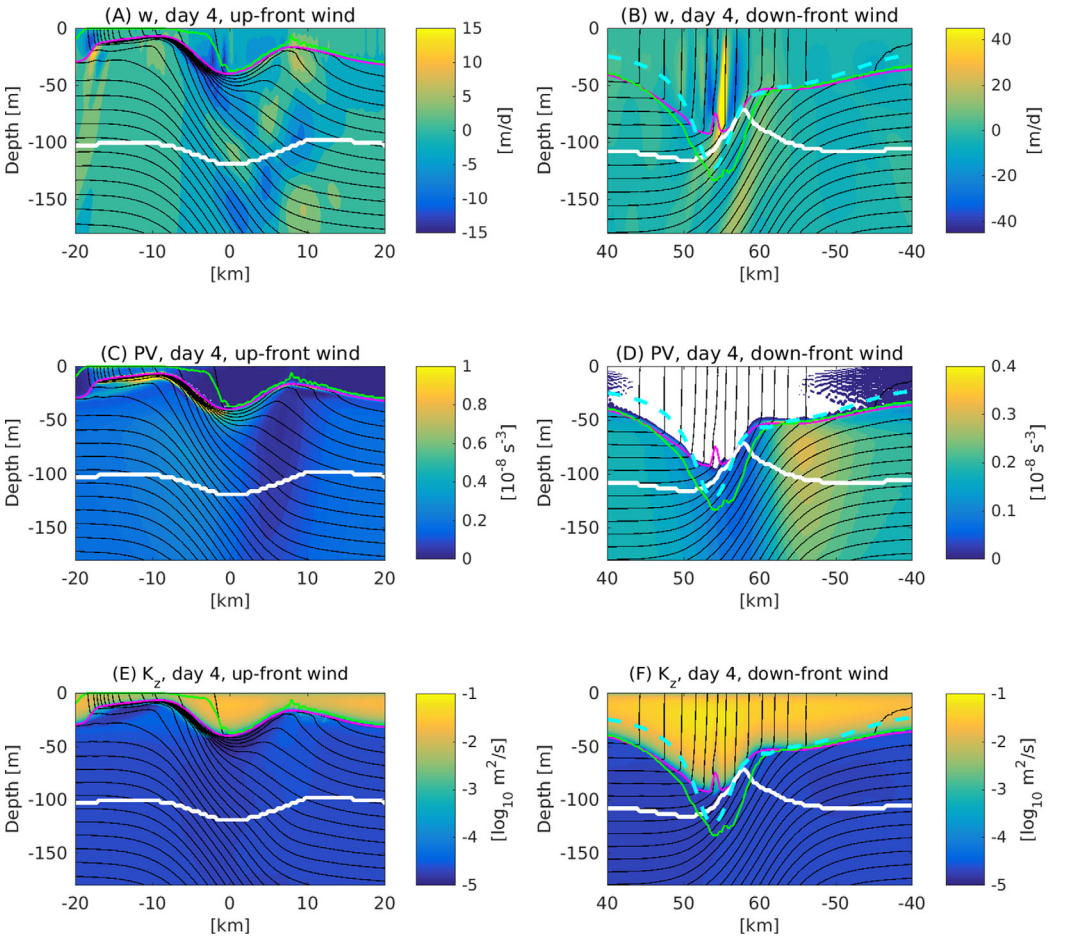

Figure 3. Snapshots of several physical variables on day 4 of the CW scenario. (left) The front centered at $y = 0$ km, where the wind points up-front, and (right) the front centered at $y = \pm 60$ km, where the wind points down-front. (a and b) Vertical velocity (note the different color bar axes), (c and d) potential vorticity (PV) q/f (q is defined in (4)) (negative PV is white; note the different color bar axes), and (e and f) vertical diffusivity K_z. All plots have density contoured every.025 kg/m^3 in black, the depth of the $N = 15$ mmol/m^3 nutrient isopleth $H_{N=15}$ in white, the high-diffusivity SBL depth from KPP H_{sbl} in magenta, the theoretically predicted low-PV layer $H_{\bar{q}}$ in cyan dashes (derived by integrating (6)), and the simulated low-PV layer depth $H_{\bar{q}}$ in green line.

The cross-front average P_{int} increases with time in both fronts in the CW simulation. However, the cross-front-average P_{int} increases more rapidly at the front forced by down-front wind compared to the front forced by up-front wind (cf., Figures 2g and 2h). In fact, after 8 days of down-front wind, P_{int} is 10–15 times larger on the less dense side of the front than outside the front or at the initial time (Figure 4f). In contrast, after 8 days of up-front wind P_{int} is at most a factor of 2 larger than outside the front (supporting information Figure S12 shows the same plots as Figure 2, but after 8 days; the results are qualitatively similar but the net biogeochemical impacts of the vertical transport are greater).

Down-front wind induces a greater increase in P_{int} than up-front wind because there is a large and sustained vertical flux of nutrient into the SXL on the less dense side of the front after about 4 days of down-front wind, which does not occur under up-front wind (see Figures 2 and 3 and supporting information Figure S12). The nutrient flux to the SXL under down-front wind can be categorized into two types in this simulation: (1) an entrainment flux of nutrient into the highly-diffusive SBL (Figures 3f and 4e), see Appendix A for a precise statement of the definition of entrainment, which is essentially the same as in *Stevenson and Niiler* [1983]), and (2) a vertical advective flux associated with narrow cells of strong upwelling and downwelling characteristic of forced SI (Figures 3b and 4d). Both types of flux depend sensitively on the depth of the SXL.

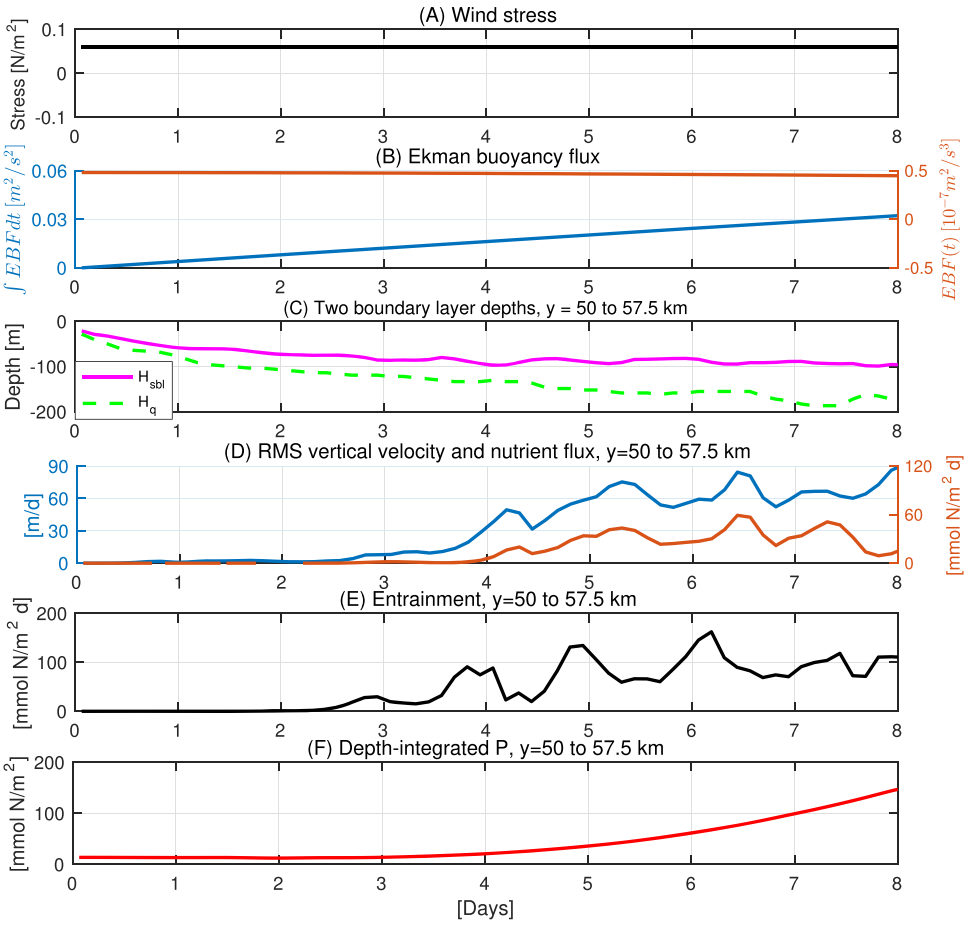

Figure 4. Time series of physical and biogeochemical variables at the front forced by down-front wind in the CW scenario. (a) The wind stress τ_x and (b) the Ekman buoyancy flux *EBF* (defined in (3)) averaged from $y = 40$ to -40 km. (c–f) Focus on the less dense side of the front, where the surface mixing layer is deepest (i.e., from $y = 50$–57.5 km, see Figure 2d). (c) The deepest SBL depth H_{sbl} (magenta) and deepest low-PV layer depth $H_{\tilde{q}}$ (green), (d) the root-mean-square (rms) vertical velocity $\sqrt{(w-w^p)^2}$ (blue) and nutrient flux $(w-w^p)(N-N^p)$ (red) associated with narrow SI cells (see also Figure 3b), (e) the mean nutrient entrainment flux $\mathcal{F}^+_{en}$ (see (A10)), and (f) the mean depth-integrated phytoplankton P_{int}. In Figure 4c, the perturbations are from fourth order polynomial fits to $w(y)$ and $N(y)$ over $y = 50$–57.5 km at each 3 h time interval, which are indicated by a superscript p. The mean values of the rms vertical velocity and vertical nutrient flux over model depth levels from $z = -80$ to -55 m are plotted in Figure 4c.

The SXL is deeper in the front forced by down-front wind primarily because the Ekman buoyancy flux,

$$EBF = \frac{-\tau_x}{\rho f}\frac{\partial b}{\partial y}, \tag{3}$$

reduces the buoyancy and stratification at the front forced by down-front wind, whereas the *EBF* increases the buoyancy and stratification at the front forced by up-front wind [e.g., *Franks and Walstad*, 1997; *Thomas*, 2005; *Thomas and Ferrari*, 2008; *Taylor and Ferrari*, 2010; *Mahadevan et al.*, 2010]. *Taylor and Ferrari* [2010] suggest a mathematical model for the depth of the SXL at a spatially uniform front (i.e., with constant initial $\partial b/\partial y$ and $-\partial u/\partial y = 0$). However, the model of *Taylor and Ferrari* [2010] fails to completely characterize either the magnitude or the spatial structure of changes in the SXL that occur in the CW simulation due to cross-front variations in e.g., $\partial b/\partial y$ and $-\partial u/\partial y$ at an isolated front (see supporting information Figure S11).

3.1.1. Modeling Entrainment at an Isolated Front

To address the limitations of the model for SXL deepening given by *Taylor and Ferrari* [2010], a new model for SXL deepening under a destabilizing *EBF* is derived in Appendix B, which adds the essential physics associated with cross-front variations in the vertical vorticity of the frontal jet to the model given by *Taylor and Ferrari* [2010]. In this model, the SXL depth is defined to be the deepest depth $H_{\tilde{q}}$, over which the depth-integrated potential vorticity (PV)

$$q = f\left(f - \frac{\partial u}{\partial y}\right)\frac{\partial b}{\partial z} + f\frac{\partial u}{\partial z}\frac{\partial b}{\partial y} \tag{4}$$

is zero, that is

$$\int_{H_{\bar{q}}}^{0} q\, dz = 0, \tag{5}$$

which is shown in Figure 3 (note that $H_{\bar{q}}$ is defined to be negative and is referred to as the low-PV layer). This low-PV definition of the SXL is motivated by the idea that wind-driven turbulent mixing in the SXL and down-front winds in particular induce negative PV (e.g., Figure 3d), which is restored toward zero on a relatively short timescale $\lesssim 1/f$ by SI [e.g., *Hoskins*, 1974; *Thomas*, 2005; *Taylor and Ferrari*, 2010] that transports high-PV water up from the pycnocline along slanted isopycnals (see Figures 3b and 3d).

The time evolution equation for $H_{\bar{q}}$ is derived by integrating the flux form of the PV equation [e.g., *Marshall and Nurser*, 1992; *Thomas*, 2005] over the depth $H_{\bar{q}}$ using the Leibniz rule and some assumptions (see Appendix B). In addition to the physical motivation based on SI, the definition (5) is also beneficial mathematically because it results in the exact elimination of explicit horizontal advective fluxes of potential vorticity by the depth-integrated cross-front flow in the low-PV layer. The resulting model represents SXL deepening due to the simultaneous action of Ekman suction [e.g., *Stern*, 1965; *Niiler*, 1969; *Stern*, 1975] and entrainment due to SI [e.g., *Straneo et al.*, 2002; *Taylor and Ferrari*, 2010]. The associated differential equation,

$$\frac{\partial H_{\bar{q}}}{\partial t} = w_{Ek} + w_{en} = \underbrace{\frac{\partial M_{Ek}}{\partial y}}_{\text{suction velocity}} + \underbrace{\frac{f^2 EBF}{q(H_{\bar{q}})H_{\bar{q}}}}_{\text{entrainment velocity}}, \tag{6}$$

can be integrated to obtain $H_{\bar{q}}(y,t)$ assuming $\partial u/\partial y$, $\partial b/\partial y$ and $q(H_{\bar{q}})$ are known functions of y and the initial $H_{\bar{q}}(y)$ is also known. Solutions can be written in closed form using the Lambert $\mathcal{W}$ function [*Corless et al.*, 1996] or obtained via numerical integration. Once $H_{\bar{q}}(y,t)$ is obtained, one can obtain the time-integrated entrainment velocity at any time t, i.e., $\int_0^t w_{en}(y,s)ds$, which is directly related to the time-integrated flux of water across the base of the low-PV layer.

Comparing the predicted depth $H_{\bar{q}}$ from (6) to the simulated depth $H_{\bar{q}}$ from the CW simulation provides a means for testing the applicability of the approximations that lead to (6). In order to apply (6) to the CW simulation, the coefficients are obtained from the initial $u(y)$, $b(y)$, and $q(y)$ at $z = -100$ m, and the stratified Ekman depth of *Pollard et al.* [1972], $H_{\bar{q}}(t=0) = H_{Ek} = -1.7\sqrt{|\tau_x|/\rho Nf} = -20$ m, is used as an initial condition. With those inputs, the theoretically predicted $H_{\bar{q}}(y, t=4 \text{ days})$ after four days of down-front wind is shown in Figure 3. The theoretical prediction is qualitatively consistent with the values for $H_{\bar{q}}$ obtained from the CW simulation over the same time period, which suggests that the theoretical model for $H_{\bar{q}}$ provides useful information about the essential physics of the response to down-front winds in the CW simulation.

The success of the full model (6) compared to reduced forms of (6) that neglect either Ekman suction or cross-front variations in relative vertical vorticity (see supporting information Figure S11), suggests that both $H_{\bar{q}}$ and the associated time-integrated entrainment velocity $\int_0^t w_{en}(s)ds$ depend significantly on $w_{Ek}(y)$ and $-\frac{\partial u}{\partial y}(y)$ in the CW simulation. Indeed, supporting information Figure S11 shows that the effects of cross-front variations in relative vertical vorticity shift the cross-front location of the deepest SXLs toward the less dense side of front by about 7 km and deepen the deepest SXLs by more than 50% after 4 days in the CW simulation. Moreover, the effects of variable vertical vorticity in (6) result in a doubling of the magnitude of the maximum time-integrated entrainment velocity over 4 days, i.e., $\max_y|\int_0^{t=4} w_{en}(s)ds|$, which depends on the vertical vorticity explicitly via $q(H_{\bar{q}})$ (as in (4)) and implicitly via $H_{\bar{q}}$. A more detailed analysis of the physics of the interaction between Ekman suction and entrainment at a front is beyond the scope of this paper and will be reported elsewhere. However, the following section uses the results of the CW simulation and the mathematical model (6) to develop a more general list of conditions that facilitate a strong phytoplankton response to a wind event at a front.

3.2. Conditions Favoring Phytoplankton Biomass Accumulation in Response to Wind at a Front

The CW simulation considered here demonstrates that a modest-amplitude wind event, characteristic of synoptic-to-planetary scale atmospheric variability, can significantly enhance nutrient fluxes to the euphotic

zone and phytoplankton biomass at a front in a nutrient limited ocean. It may be noted that the depth and gradient of the nutricline, which depend on the parameters of the biogeochemical model (see section 2.2 and supporting information section S4.1), are crucial factors that precondition the response of P_{int} to vertical transport. In particular, both Ekman suction and wind-driven mixing are associated with surface-intensified vertical transport (Figure 3), so the upward flux of nutrients due to either process depends sensitively on the depth and gradient of the nutricline. Furthermore, even under identical physical and biogeochemical initial conditions, the spatial distribution and magnitude of the change in P to a wind event differs substantially depending on the wind direction (Figure 2 and supporting information Figure S12), which significantly impacts vertical transport at a front (Figure 3). The remainder of this section synthesizes the simulation results and theory into a summary of the physical conditions that facilitate deep SXLs, strong Ekman suction velocities and hence larger nutrient fluxes and more phytoplankton biomass accumulation at fronts forced by winds in nutrient-limited oceans.

In the CW simulation, the largest increases in P_{int} occur where nutrient is entrained into deep SXLs at the front forced by down-front wind, because boundary layer turbulence drives much larger vertical tracer fluxes than Ekman suction. These specific results support a more general hypothesis: fronts modulate the SXL depth and deeper SXLs are associated with enhanced nutrient fluxes and enhanced phytoplankton growth in nutrient limited conditions. Three physical ingredients facilitate deeper wind-driven SXLs and hence enhanced vertical nutrient fluxes via turbulent mixing at fronts:

1. strong and/or sustained down-front winds,
2. strong horizontal buoyancy gradients at the surface, and
3. low potential vorticity just below the SXL.

Together these three physical ingredients are associated with both large and negative time-integrated entrainment velocities $\int_0^t w_{en}(s)ds$ and hence deeper SXLs. The first two ingredients are associated with large time-integrated Ekman buoyancy fluxes $\int_0^t EBF(s)ds$ (EBF is defined in (3)), that is greater losses of buoyancy due to the cross-front Ekman transport. Low potential vorticity (defined in (4))—due to low stratification, strong anticyclonic vertical vorticity ($-\partial u/\partial y \sim -f$), and/or steep isopycnal slopes—increases the sensitivity of the SXL depth to wind-driven buoyancy loss via EBF.

In the CW simulation, Ekman suction is the primary contributor to the total phytoplankton response in the front forced by up-front wind. At this front, SXLs do not reach the nutricline, and the vertical tracer fluxes associated with Ekman suction are larger than those associated with the weak parameterized turbulent mixing in the pycnocline (where $K_z \approx 2\times10^{-5}$ m^2/s). Although the fronts are associated with both upwelling and downwelling (i.e., suction and pumping), the increase in P_{int} due to Ekman suction (i.e., upwelling) is greater than the decrease in P_{int} due to Ekman pumping (i.e., downwelling), hence the cross-front-averaged P_{int} increases in both fronts. These results support another more general hypothesis: where the SXL is shallower than the nutricline, Ekman suction drives upwelling and advective nutrient flux to the euphotic zone below the SXL and therefore enhances phytoplankton growth at the SPM at fronts in nutrient limited conditions. Three physical ingredients facilitate stronger Ekman suction velocities at fronts:

1. strong/sustained along-front wind stress,
2. large spatial variations in the absolute vertical vorticity of the frontal jet, and
3. a small SXL depth relative to the depth of the frontal jet.

Together, these three physical ingredients are associated with larger wind-driven vertical displacements below the SXL due to Ekman suction, i.e., $\int_0^t w_{Ek}(s)ds$. The first ingredient is associated with large cross-front Ekman transports, whereas the second two ingredients cause the cross-front Ekman transport to be divergent. The last condition, which holds in the simulation but not always in the real ocean, is not a consequence of (1), but rather is a required assumption made during the construction of the Ekman suction model (see section 8.2 of *Stern* [1975]).

4. Oscillatory Wind

In the real ocean, the Ekman suction velocity and Ekman buoyancy flux vary in time, primarily due to changes in the wind stress direction and amplitude, but also due to temporal variations in the spatial orientation of the fronts in the ocean [e.g., *Thomas et al.*, 2016; *Thompson et al.*, 2016]. Hence, a question arises:

what is the time-integrated effect of synoptic-to-planetary-scale wind oscillations on entrainment, pumping/suction, nutrient fluxes, and phytoplankton biomass distributions at a front? The definitions of w_{Ek} (2) and *EBF* (3) integrate to zero if the background horizontal buoyancy and velocity gradients are assumed constant in time and the wind stress integrates to zero. If, in addition, the potential vorticity in the pycnocline is assumed to be constant in time, then the time-integrated change in $H_{\bar{q}}$ in (6) is also theoretically zero. Hence, the time-integrated physical and biogeochemical effects of an oscillatory spatially uniform wind stress over a front are expected to be small to a first approximation. However, the CW simulation results show that the large increase in P_{int} in response to a transient period of down-front wind is associated with irreversible turbulent mixing, which suggests that oscillating along-front winds with zero time-mean stress might have a substantial impact on biogeochemistry at a front due to deep mixing in the SXL that occurs when the wind stress is pointed down-front. In addition, persistent oscillatory vertical transport may induce changes in the time-averaged partitioning of $N_{int}+P_{int}+Z_{int}+D_{int}$ between the four biogeochemical constituents due to nonlinearities in the biogeochemical reactions.

This section explores the physical and biogeochemical response to oscillatory winds with frequencies and amplitudes characteristic of synoptic-to-planetary scale atmospheric variability using the same 2-D model configuration used in section 3. The analysis focuses primarily on one simulation, which is forced by an oscillatory along-front wind stress $\tau_x = .18\cos(.09ft)$ N/m^2 with an 8 day period (the equivalent peak wind speed is about 10.5 m/s at 10 m height), although some other 2-D sensitivity simulations are also presented. This primary simulation is labeled XW (for *x* winds) in Table 1.

4.1. Description of the XW Simulation

The maximum magnitude of the wind stress in the XW simulation is 3 times larger than in the CW simulation (0.18 compared to.06 N/m^2) and the equivalent maximum magnitude of the wind speed at 10 m height is about 70% greater in the XW simulation than the CW simulation (10.5 compared to 6 m/s). However, the wind stress is still not sufficiently strong to modify the *N* or *P* distributions via mixing in the SXL outside the front. Instead, as in the CW simulation discussed in section 3, the oscillatory XW wind induces *N* and *P* anomalies at the fronts by driving entrainment of nutrients into deep SXLs and by driving vertical displacements at the nutricline. However, because the wind is oscillatory, the two fronts in the XW simulation exhibit qualitatively similar dynamics (unlike the two fronts in the CW simulation).

4.1.1. Entrainment and Mixing in the SXL

Unlike the front forced by a steady down-front wind in the CW simulation, the SXLs are shallower in the fronts than outside the fronts at most times in the XW simulation (Figure 5). However, deeper SXLs do occur on the less dense side of the fronts in conjunction with local maxima in the time-integrated *EBF*,

$$\max_{t} \int_0^t EBF(s)ds, \tag{7}$$

which occur after periods of down-front wind stress when the buoyancy and stratification at the front are lowest, for example at $t = 6$ days in the front centered at $y = 0$ km (Figures 5 and 6). In particular, the first maximum of $\int_0^t EBF(s)ds$ at $t = 6$ days coincides with the deepest SXLs, SI, and large entrainment, all of which lag the first maximum in the down-front wind stress and *EBF* by 2 days in the XW simulation (Figure 6).

The physical and biogeochemical state of the front centered at $y = 0$ km in the XW simulation at $t = 6$ days is similar to the state of the front forced by down-front wind in the CW simulation at $t = 4$ days because the time-integrated *EBF* is about the same in both cases, that is $\int_0^{4d} EBF_{CW}(s)ds \approx \int_0^{6d} EBF_{XW}(s)ds$. At these times, the deepest SXLs are in a similar location and achieve a similar deepest depth on the less dense side of the front (cf., Figures 2d and 5b), the vertical velocity variance and advective nutrient flux associated with SI occur in a similar *y* location and have a similar magnitude (cf., Figure 4d with 6d), *P* has a similar spatial structure (cf., Figures 2d and 5b), and P_{int} increases by a similar magnitude compared to the initial time on the less dense side of the front (cf., Figures 4f and 6f). These qualitative and quantitative similarities highlight the significance of the maxima in the time-integrated *EBF* (7) for deep SXLs at fronts, in support of the results of section 3.2. However, under the oscillatory XW wind, the value of the time-integrated *EBF* depends crucially on the *phase* of the wind stress, not merely the total duration and magnitude of the stress as in the CW simulation (cf., Figures 4 and 6). These results suggest that the biogeochemical response to oscillatory wind may be highly sensitive to both the amplitude and frequency of the wind stress, because lower frequencies and higher amplitudes will both yield a larger maximum time-integrated *EBF*, which leads to

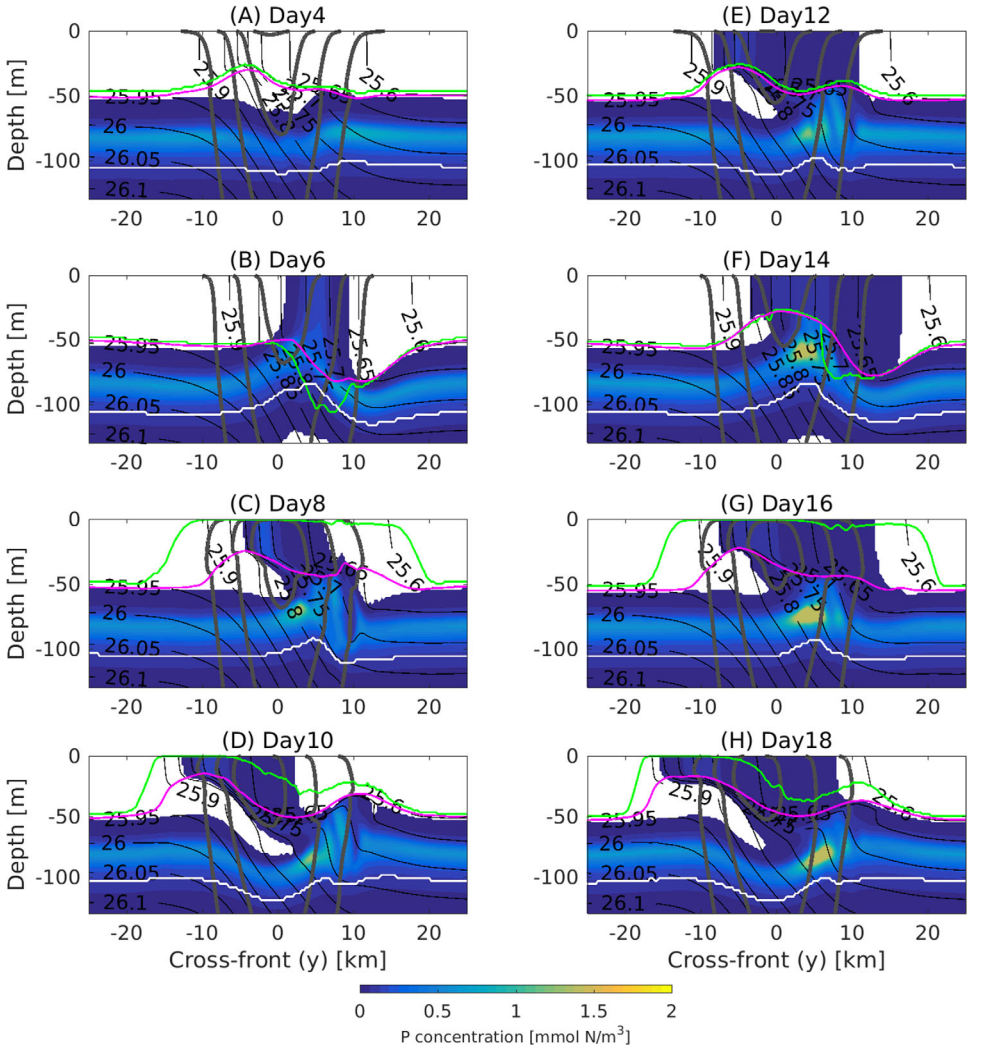

Figure 5. Snapshots over the first 18 days of the XW simulation: phytoplankton concentration (color), density (black contours), along-front velocity (thick gray contours every 0.2 m/s; the jet points into the page and the zero contour is not shown), low-PV layer depth (defined in section 3, green lines), SBL depth (defined by KPP, magenta lines), and the nutricline depth (i.e., the $N = 15$ isopleth of nutrient, white lines). Time series of the wind stress, Ekman buoyancy flux, and time-integrated Ekman buoyancy flux are plotted in Figures 6a and 6b. Note that phytoplankton concentrations $P < 10^{-2}$ mmol N/m^3 appear as white.

deeper mixing and a greater biogeochemical response on the less dense side of the front in a single (transient) down-front wind event (Figure 4). Hence, sensitivity simulations with different wind stress periods (4–16 days) and amplitudes (0.06–0.24 N/m^2) were conducted (see Table 1). The qualitative results of the sensitivity simulations are similar to those of the primary XW simulation in that the deepest SXLs occur in conjunction with the first maximum in $\int_0^t EBF(s)ds$ and lag the maximum in the down-front wind stress and *EBF*. In addition, lower-frequency and higher amplitude stresses are associated with deeper SXLs on the less dense side of the front, although the relationship is nonlinear (see supporting information section S6).

However, in the primary XW simulation and all the sensitivity XW simulations, physical adjustments between the first and subsequent forcing periods result in substantially shallower SXLs and less nutrient entrainment at the second and subsequent maxima in $\int_0^t EBF(s)ds$ (at $t = 14, 22, \ldots$ days, see Figure 6 and section S6). In addition, both the PV at the SXL base and the horizontal buoyancy gradient in the boundary layer vary significantly within a forcing period (see Figure 5; in addition, supporting information Figure S3 shows several snapshots of the vertical velocity and PV during the first 19 days of the XW simulation). These changes to the coefficients in (6) within a forcing period introduce physical hysteresis (i.e., memory) that acts to suppress nutrient entrainment and SI in the SXL after the first period of oscillatory along-front wind. More generally, this hysteresis acts to reduce the effectiveness of SXL mixing relative to expectations based

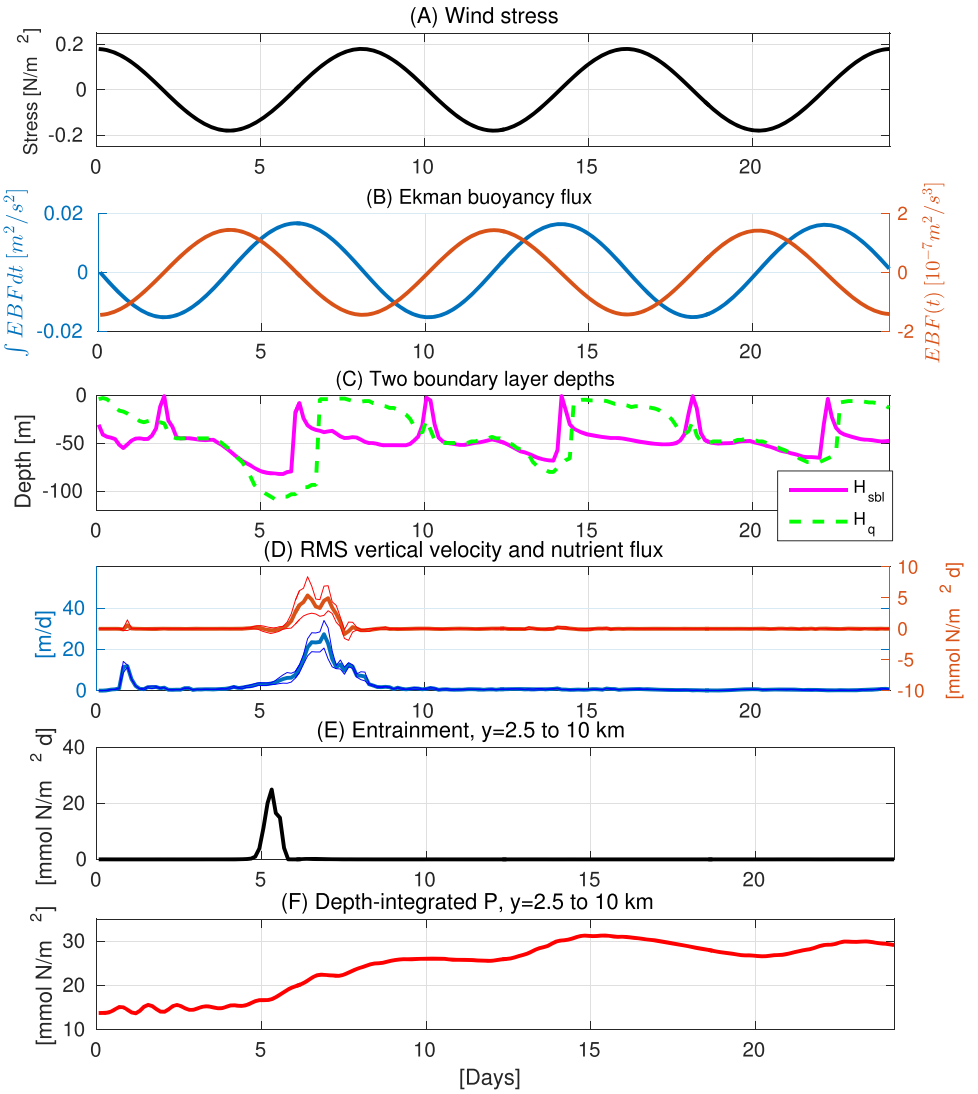

Figure 6. (a) Wind stress, (b) Ekman buoyancy flux (defined in (3)) (red) and time-integrated Ekman buoyancy flux (blue) both averaged from $y = -20$ to 20 km, (c) deepest depths of the low-PV layer $H_{\tilde{q}}$ (defined in (5)) and surface mixing layer H_{sbl} (from $y = 2.5$ to 10 km), (d) the root mean square (RMS) vertical velocity $\sqrt{(w-w^p)^2}$ (blue line) and perturbation nutrient flux $(w-w^p)(N-N^p)$ (red line) associated with the high horizontal wave number SI from $y = 2.5$ to 10 km (see supporting information Figure S3), (e) the nutrient entrainment flux (defined in section 3) averaged from $y = 2.5$ to 10 km, and (f) P_{int} averaged from $y = 2.5$ to 10 km. In Figure 6c, the perturbations are from fourth-order polynomial fits to $w(y)$ and $N(y)$ over $y = 2.5$ to 10 km at each model depth level from $z = -80$ to -55 m and each 3 h time interval. The mean values of the RMS vertical velocity and vertical nutrient flux over all depth levels (thick line) and plus/minus one standard deviation (thin lines) are plotted in Figure 6c.

on the results of section 3, which would naively imply that the first and subsequent forcing periods would be the same. In any case, SXL mixing contributes minimally to the biogeochemical dynamics after the first forcing period in the primary XW simulation, hence the remainder of section 4 focuses on how the oscillatory winds drive vertical advection in the pycnocline and thereby modify N and P in the XW simulation.

4.1.2. Advection and Biogeochemical Dynamics Below the SXL

Although vertical mixing in the SXL does not drive strong vertical nutrient fluxes after the first forcing period, the phytoplankton concentration at the SPM and depth-integrals of all three biogeochemical constituents, i.e., P_{int}, Z_{int}, and D_{int}, remain elevated by about a factor of two after nine forcing periods (72 days) on the less dense side of the front (Figures 7c, 7d, 7g, and 7h). In addition, snapshots of the phytoplankton distribution as a function of time (Figure 5) and time series of phytoplankton and nutrient anomalies on the less dense side of the front (Figures 7d and 7f) reveal strong oscillatory vertical displacements at the nutricline/SPM in the XW simulation.

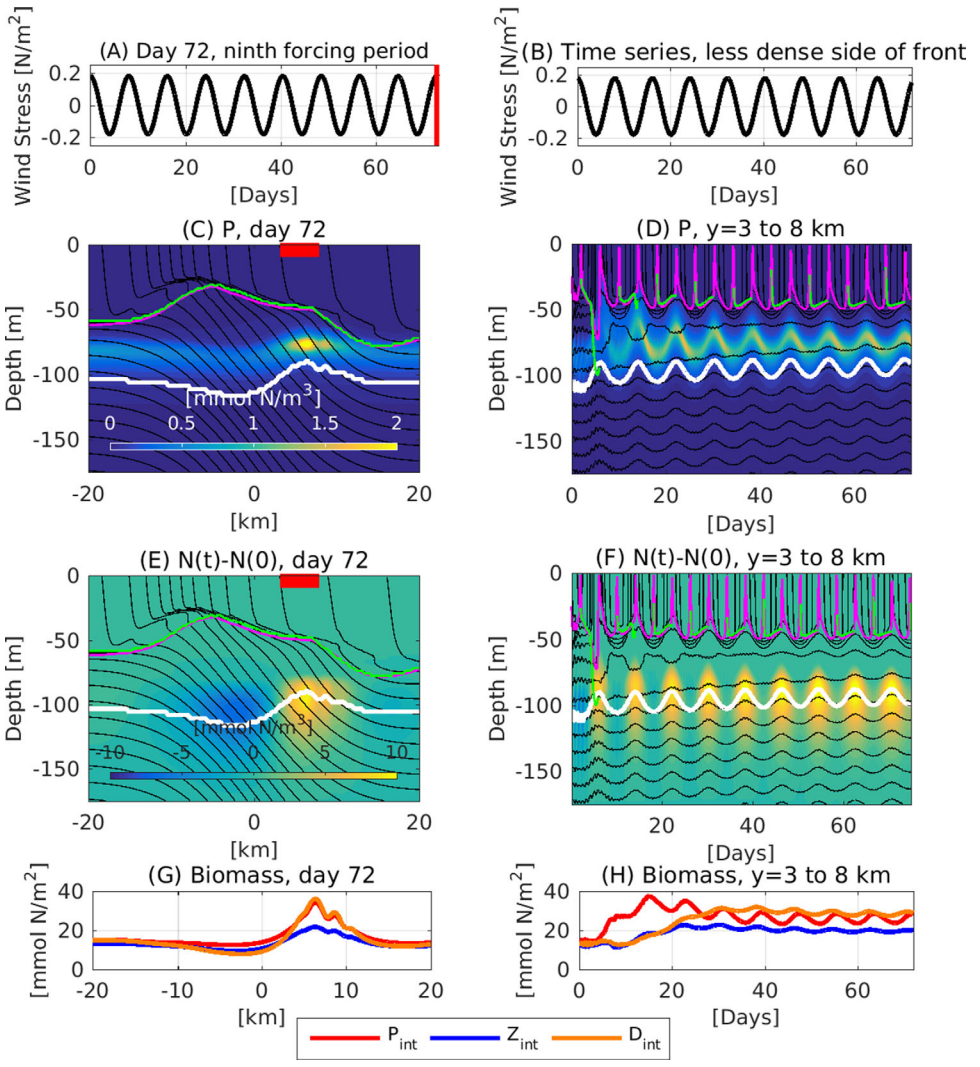

Figure 7. Snapshots (left) and time series (right) of the biogeochemical response to oscillatory along-front wind in the XW scenario. (a and b) Wind stress, (c and d) phytoplankton P, and (e and f) nutrient anomaly $N(t)-N(0)$. The red bars at $z = 0$ m in Figures 7c and 7e indicate the $y = 3$–8 km range, which is averaged to produce (d), (f), and (h). Figures 7c–7f have density contoured every.025 kg/m^3 in black, the depth of nutricline (i.e., the $N = 15$ mmol/m^3 nutrient isopleth) contoured in white, and the deepest SBL depth max $|H_{sbl}(y,t)|$ (defined by KPP) contoured in magenta as well as the deepest low PV layer depth max $|H_{\tilde{q}}(y,t)|$ (defined in section 3) contoured in green (the maxima are over $T = 64$–72 days in Figures 7c and 7e, and $y = 3$–8 km in Figures 7d and 7f). (g and h) Full-depth-integrated phytoplankton P_{int} in red, zooplankton Z_{int} in blue, and detritus D_{int} in orange as a function of y after the ninth forcing period (g) and as a function of time (h).

Vertical profiles of the advective nutrient flux convergence averaged over two wind-forcing periods (16 days), that is $\overline{-\nabla_{y,z}\cdot(\mathbf{v}N)}^{y,t}$ where the overbar denotes an average over y and t, exhibit a dipole structure with negative flux convergence on the more dense side of the front (i.e., averaged from $y = -15$ to 0 km, see Figure 8a) and positive flux convergence on the less dense side of the front (i.e., averaged from $y = 0$ to 15 km, see Figure 8b). This persistent pattern in the forcing-period-averaged advective flux (Figures 8a–8c) decays only slightly over several forcing periods on both sides of the front. Since the diffusive flux and biological remineralization profiles are only slightly modified by the forcing after the first forcing period (see Figures 8e, 8f, 8h, 8i), the convergence of the advective flux below the SPM leads to an increase in nutrient concentration (Figures 8k and 8l). Hence, the forcing-period-average depth of nutricline rises on the less dense side of the front and descends on the more dense side of the front (Figures 7e and 7f). However, at shallower depths on the less dense side of the front, some of the advective flux convergence is balanced by an increase in the net consumption of nutrients (Figures 8h and 8i), which may sustain a forcing-period-averaged increase in biomass on the less dense side of the front after the first forcing period (Figures 7c, 7d, 7g, and 7h).

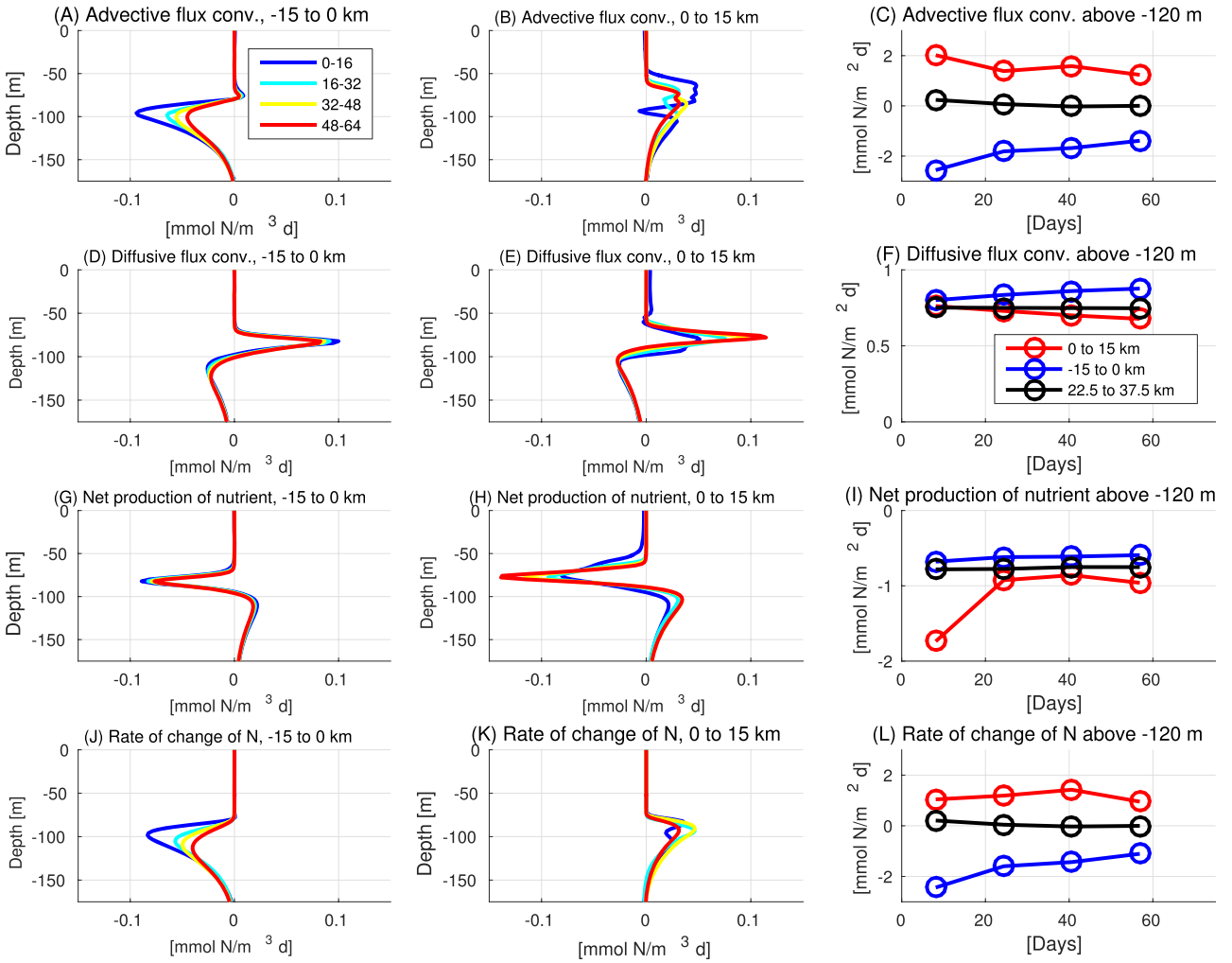

Figure 8. The four terms in the nutrient rate equation (advective flux, diffusive flux, net consumption of nutrient by biology, and rate of change) as a function of time and space. The left and middle columns show time and horizontally averaged vertical profiles on the more dense ($y = -15$ to 0 km) and less dense ($y = 0$–15 km) sides of the front, respectively. The numbers and line color in the legend in Figure 8a indicate the averaging time for each vertical profile in the left two columns of plots. The right column shows time series of the same four terms after depth-integrating from $z = -120$ m to 0. Different line colors are associated with different horizontal averages, as indicated in the legend in Figure 8f.

Two hypotheses may explain the forcing-period-averaged nutrient flux and increase in biomass on the less dense side of the front in the XW simulation:

1. oscillatory vertical transport sustains more biomass on the less dense side of the front due to nonlinearities in the biogeochemical reactions, and/or
2. a residual forcing-period-averaged vertical transport sustains enhanced biomass on the less dense side of the front.

The following section explores these hypotheses by using both 1-D and 2-D simulations to separate the biogeochemical effects of oscillatory and time-mean vertical transport in the XW simulation.

4.2. Separating the Biogeochemical Effects of Oscillatory and Time-Mean Vertical Transport

The results of the previous section show that the less dense sides of the fronts are associated with significant oscillatory vertical displacements, a forcing-period-averaged advective nutrient flux to the euphotic zone, and a sustained increase in biomass in the XW simulation. However, the relative importance of the large oscillatory vertical displacements and the smaller time-mean vertical transport is unclear. This section uses the results of the 1-D simulations described in section 2.4 to explicitly separate the biogeochemical impacts of the large oscillatory vertical displacements from the biogeochemical impacts of small forcing-period-averaged vertical displacements, both of which may contribute to the forcing-period-averaged

nutrient flux and enhanced biomass on the less dense side of the front in the XW simulation. In addition, a 2-D sensitivity simulation is used to separate the biogeochemical effects of spatially and temporally variable vertical diffusion of biogeochemical variables from all other sources of biogeochemical transport in the XW simulation (including advective transport of biogeochemical variables driven by variable diffusion of density and viscosity, which will be discussed in section 4.3 below).

4.2.1. Oscillatory Displacements

The oscillatory vertical displacements in the XW simulation can be qualitatively and quantitatively explained using the Ekman suction model of *Stern* [1965]. In particular, oscillatory along-front winds drive oscillatory cross-front Ekman transport $M_{Ek}(t)$ (defined in (2)), which drives oscillatory Ekman suction w_{Ek} (defined in (1)), and hence oscillatory vertical displacements:

$$\zeta_{Ek}(t)=\int_0^t w_{Ek}(s)\,ds=\int_0^t \frac{\partial}{\partial y}\left(-\frac{\tau_x}{\rho(f-\partial u/\partial y)}\right)=\frac{\partial}{\partial y}\left(-\frac{A\sin(\omega t)}{\omega\rho(f-\partial u/\partial y)}\right), \tag{8}$$

where A =.18 N/m^2, ω=.09f. It may be noted that the time when $|\zeta_{Ek}|$ is maximum coincides with the time when the wind stress magnitude is minimum and therefore the time when $|M_{Ek}|$ is minimum. In addition, ζ_{Ek} averages to zero over an 8-day forcing period $2\pi/\omega$ by design. The resulting vertical displacements ζ_{Ek} manifest as oscillatory displacements of the SPM and nutricline depth (see Figure 9). For example, local maxima in $|\zeta_{Ek}|$ occur at t = 6, 10, 14, and 18 days, as shown in Figures (5 and 7)d and 7f. The root-mean-square (RMS) vertical velocity at −33 m and the RMS cross-front transport in the SBL, that is $M_{H_{sbl}}=\int_{H_{sbl}}^{0} v\,dz$, are similar in magnitude and spatial structure to the theoretical predictions for w_{Ek} and M_{Ek}, respectively, which are derived from Ekman theory (i.e., (8)) (supporting information Figure S13). In particular, the RMS vertical velocity exhibits a tripolar structure with the largest peak in the middle of the front, where the RMS $w_{Ek} \approx 10-15$ m/d, and two smaller peaks at the flanks of the front, i.e., near $y=\pm12$ km, where the RMS $w_{Ek} \approx 5-10$ m/d. Time series of virtual Lagrangian drifters initialized at $z=-105$ m show that this oscillatory Ekman suction is associated with a tripolar pattern of oscillatory vertical displacements with an amplitude $|\zeta| \sim 10$ m, consistent with (8) (Figure 9a).

In the 1-D biogeochemical simulations with vertical advection by the oscillatory part of the vertical velocity from Lagrangian drifters, that is $w(t)-\langle w\rangle$ (see section 2.4), the full-depth-integrated biomass $B_{int}=P_{int}+Z_{int}+D_{int}$ changes rapidly during the first two forcing periods (solid green lines in the top row of plots in Figure 10). The magnitude of the transient changes in biomass during the first two periods of the oscillatory displacements vary with the magnitude of the oscillatory vertical displacements (e.g., at y = 3 and 5 km in Figure 10). However, the oscillatory part of the vertical advection does not drive a sustained increase in B_{int} at any cross-front location tested. In all four 1-D simulations shown in Figure 10 (i.e., at cross-front locations

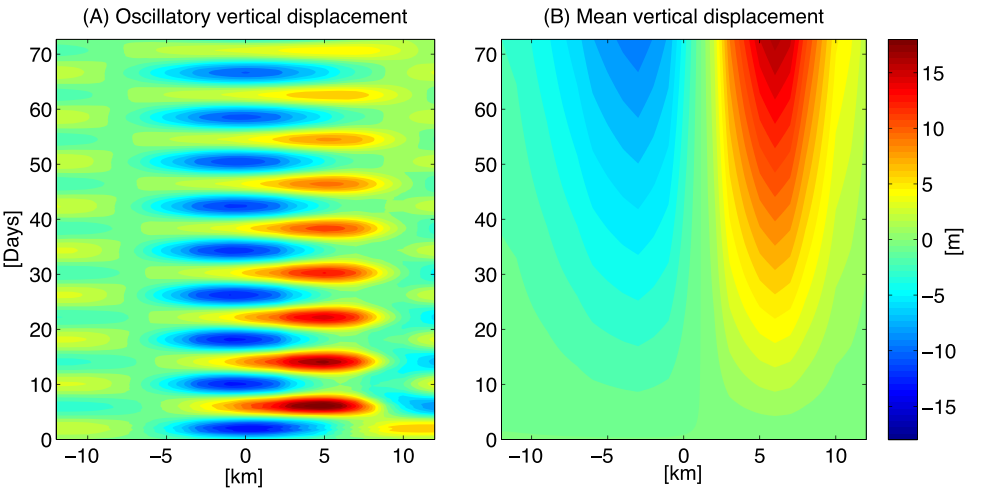

Figure 9. (a) Oscillatory $\zeta(t)-\langle\zeta(t)\rangle$ and (b) mean $\langle\zeta(t)\rangle$ vertical displacements of the Lagrangian drifters seeded at $z=-105$ m. The "mean" is computed by time integrating the mean vertical velocity $\langle w(t)\rangle$, which is computed by time-averaging over the first nine forcing periods (72 days) of $w(t)$. The results do not depend strongly on the precise definition of the average $\langle\rangle$; see supporting information Figure S4 for the raw drifter positions and supporting information Figure S5 for the same variables that are plotted here but with a different definition for $\langle\rangle$.

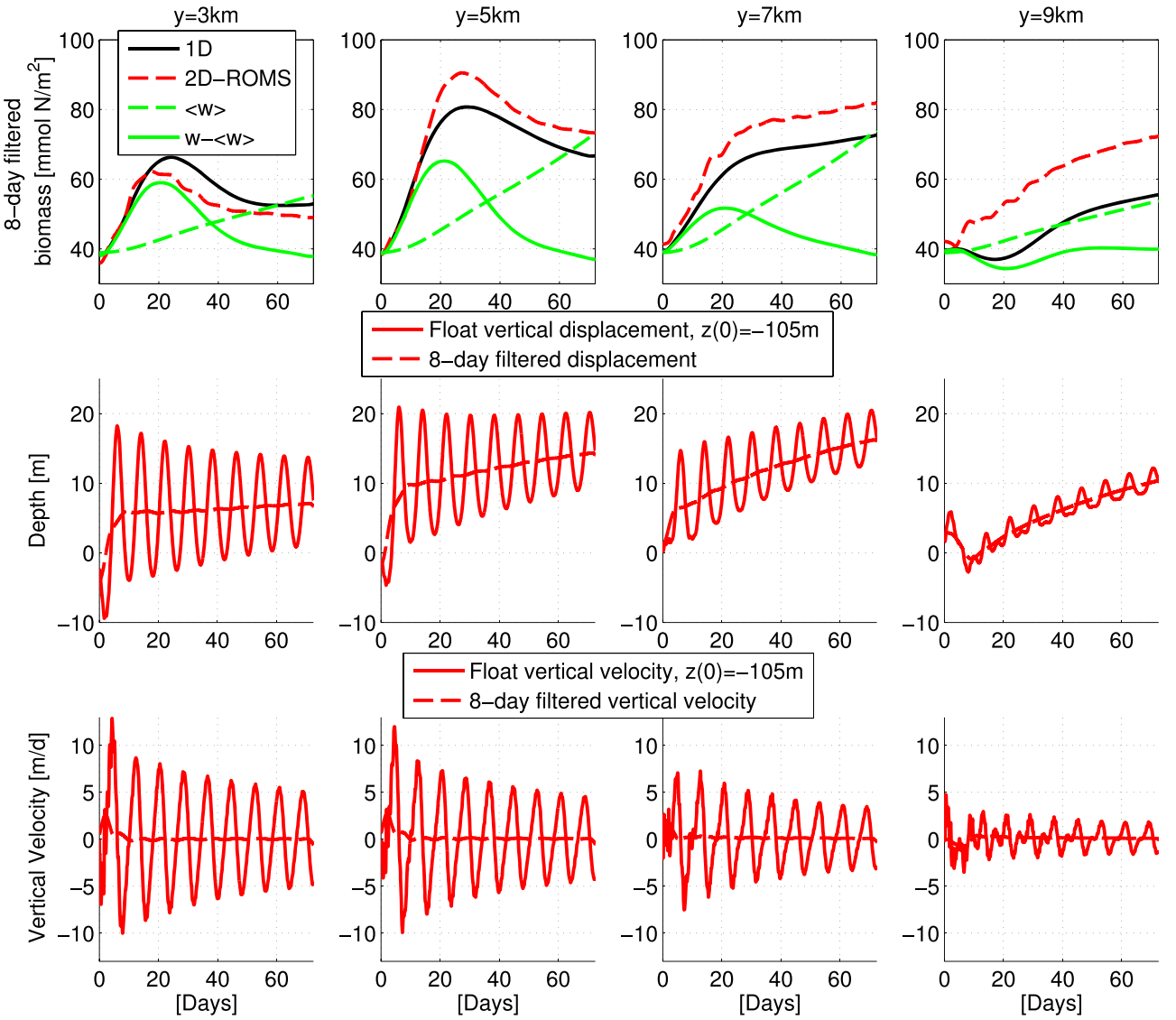

Figure 10. The top row of plots show the depth-integrated and time-filtered (8 day moving average) biomass $B_{int}=P_{int}+Z_{int}+D_{int}$ at $y=3$, 5, 7, and 9 km (as indicated in the titles). The red-dashed line indicates the value obtained from the primary 2-D simulation (XW), the black solid line indicates the value obtained from the 1-D simulation with vertical advection by the time-filtered Lagrangian drifter velocity initialized at $z=-105$ m, at $t=0$, and at the cross-front y location indicated in the title. The green-dashed line indicates the value obtained from the 1-D simulation with vertical advection by only the time-average drifter velocity $\langle w\rangle$, and the green solid line indicates the value obtained from the 1-D simulation with vertical advection by only the oscillatory perturbation drifter velocity $w-\langle w\rangle$. The middle and bottom rows of plots show the associated time-filtered vertical displacement $\zeta(t)-\zeta(0)$ (middle) and vertical velocity $w(t)=d\zeta/dt$ (bottom) of the drifters at the cross-front position y indicated in the title of the top plot in the column. The solid red lines indicate a 2 day moving averages, whereas the dashed red lines indicates an 8 day moving averages.

$y=3$, 5, 7 and 9 km), B_{int} is near to or lower than its initial value after 9 forcing periods of oscillatory vertical advection. Therefore, although the oscillatory vertical advection results in larger oscillatory vertical displacements and can contribute to the rapid increase in biomass during the first two forcing periods observed in the XW simulation (Figures 5 and 6), the oscillatory vertical displacements cannot explain the presence of elevated biomass on the less dense side of the front at nine forcing periods (Figure 7).

4.2.2. Mean Displacements

In addition to the strong oscillatory vertical velocity ($w_{Ek}\sim 10$ m/d), the oscillatory along-front wind induces a smaller mean vertical velocity $\langle w\rangle\sim 0.1-0.2$ m/d at the nutricline, which manifests as a slow forcing-period-averaged drift in the depth of the virtual Lagrangian drifters initialized at $z=-105$ m (Figure 9b; the Lagrangian mean $\langle\rangle$ is defined in section 2.4). These Lagrangian mean vertical displacements $\langle\zeta\rangle(t)=\int_0^t\langle w\rangle ds$ exhibit a dipolar cross-front structure (Figure 9b), with upwelling on the less dense side of the front and downwelling on the more dense side of the front, similar to the cross-front patterns of the forcing-period-

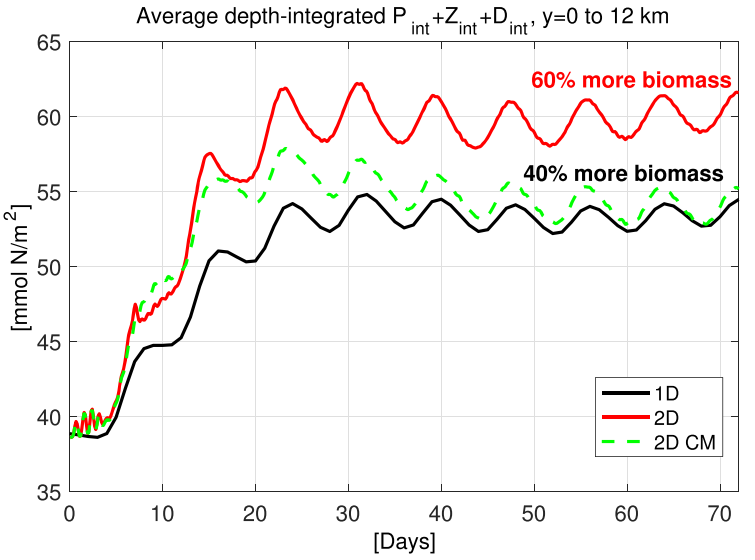

Figure 11. Average depth-integrated biomass $B_{int}=P_{int}+Z_{int}+D_{int}$ from $y=0$ to 12 km in the primary 2-D XW simulation (red) and averaged over the 13 1-D simulations (black) with vertical velocities $w(t)$ derived from Lagrangian drifters spaced across the same range of y. Stated percent increases in B_{int} are relative to the initial time. The green-dashed line indicates the average depth integrated biomass from $y=0$ to 12 km in the 2-D CM simulation (see Table 1), which is identical to the primary simulation except for the vertical diffusivity K_z applied biogeochemical variables is set to the same constant $K_z=2\times10^{-5}$ m^2/s applied to biogeochemical variables in the 1-D simulations.

averaged advective nutrient flux convergence (Figures 8a and 8b) as well as the nutrient anomaly below the SPM (Figure 7f) and B_{int} (Figure 7h) at late times.

The 1-D simulations forced by the mean vertical velocity $\langle w\rangle$ have a similar B_{int} as the 2-D simulation at $y=3$, 5, and 7 km after 72 days (c.f. the dashed green and dashed red lines in the top row of plots in Figure 10). However, at early times, the 1-D simulations forced only by $\langle w(t)\rangle$ have much smaller B_{int} than either the 2-D simulations or the 1-D simulations forced by the oscillatory part of the vertical velocity $w(t)-\langle w(t)\rangle$ (Figure 10).

On the other hand, 1-D simulations forced by both the mean and oscillatory parts of the drifter vertical velocity $w(t)$ yield a reasonably close match to B_{int} in the 2-D simulations at most cross-front locations tested (cf., the solid black lines and dashed red lines in the top row of plots in Figure 10). When averaged from $y=0$ to 12 km, the 1-D simulations reproduce the timing and approximate magnitude of the biomass increase observed in the 2-D simulation (Figure 11). However, the 1-D simulations yield only a 40% increase in B_{int} relative to the initial time, whereas the 2-D XW simulation yields a 60% increase in B_{int} relative to the initial time (Figure 11). Both spatially variable advection and spatially variable diffusion of biogeochemical variables in the 2-D simulation may contribute to this discrepancy between B_{int} in the 1-D and 2-D simulations.

The effect of variable vertical diffusion of biogeochemical variables on B_{int} is isolated from the effects of all other transport processes by comparing the XW simulation with the 2-D sensitivity simulation with constant vertical mixing of biogeochemical variables (CM, see Table 1). The CM simulation has the same physics as the XW simulation (i.e., the same time-dependent wind stress, vertical viscosity, diffusivity of density, and velocity). However, a constant diffusivity, $K_z=2\times10^{-5}$ m^2/s, is applied biogeochemical variables in the 2-D CM simulation, as in the 1-D simulations. The results show that the time-series of B_{int} averaged from $y=0$ to 12 km in the 2-D CM simulation more closely matches the time-series of B_{int} derived from the 1-D simulations than it matches the time series of B_{int} derived from the 2D XW simulation. Hence, the difference between the 40% increase in B_{int} in the 1-D simulations and the 60% increase in B_{int} in the XW simulation is primarily attributable to variable vertical diffusion of biogeochemical variables.

In summary, the oscillatory vertical advection induced by Ekman suction is the dominant physical driver of the rapid transient increase in B_{int} on the less dense side of the front during the first two forcing periods, yet the time-mean upwelling below the boundary layer is the dominant physical driver of the elevated biomass below the boundary layer on the less dense side of the front after the first two forcing periods. In addition, variable vertical diffusion of biogeochemical variables contributes to the enhanced biomass at late times, but to a lesser degree than the time mean upwelling.

4.3. Separating the Explicit Biogeochemical Effects of the Along-Front Wind Stress From the Effects of Variable Vertical Mixing of All Variables

This section builds on the results of the previous section by separating the explicit biogeochemical effects of the along-front wind stress, which drives the cross-front Ekman transport and Ekman suction, from the

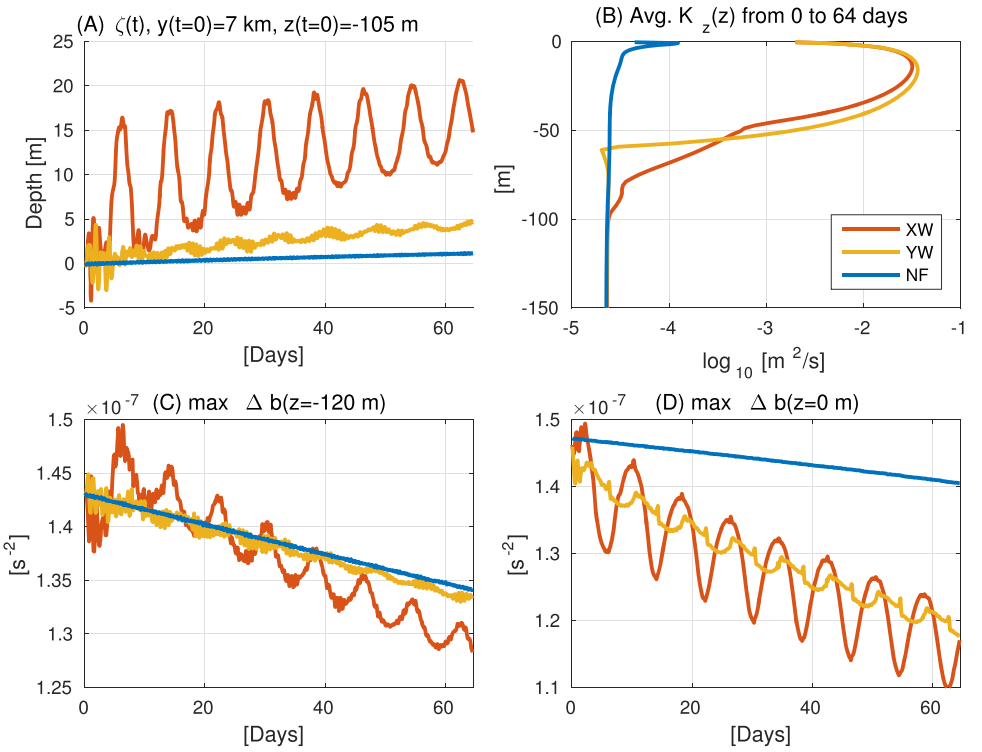

Figure 12. A comparison between three simulations with different imposed forcing parameters, as indicated in the legend in (b): (NF) no wind forcing, (XW) along-front wind stress $\tau_x = .18\cos(.09ft)$, and (YW) cross-front wind stress $\tau_y = .18\cos(.09ft)$ (the same group of simulations plotted in Figure 13). (a) The Lagrangian vertical displacement $\zeta(t)$ for a virtual drifter initialized at $z = -105$ m and $y = 7$ km, (b) the average vertical diffusivity profile $K_z(z)$ from $t = 0$ to 64 days at $y = 7$ km, (c) the maximum $\max_y \Delta b(y,t)$ at $z = -120$ m, and (d) the maximum $\max_y \Delta b(y,t)$ at $z = 0$ m, where $\Delta b(y,t) = \frac{b(y+10\ \mathrm{km},t) - b(y-10\ \mathrm{km},t)}{20\ \mathrm{km}}$ is a measure of the maximum average cross-front buoyancy gradient.

effects of the spatially and temporally variable vertical mixing of all variables, including mixing of density and momentum, which drives vertical velocities in the front [e.g., *Eliassen*, 1951; *Garrett and Loder*, 1981; *Thompson*, 2000; *Nagai et al*., 2006; *McWilliams et al*., 2015]. The separation is accomplished by comparing the XW simulation with 2-D sensitivity simulations that have similar spatially and temporally varying vertical mixing coefficients for all variables but different wind stresses. The hypothesis is that the biogeochemical response to an along-front oscillating surface stress depends more strongly on the orientation of the wind and the associated Ekman transport than the spatially and temporally variable vertical diffusivity and viscosity. A corollary to this hypothesis is that the mean vertical circulation and the associated biogeochemical response discussed in the previous section cannot be explained completely using *any* theory for vertical circulations driven by spatially and temporally variable viscosity and diffusion of density in the absence of the explicit wind stress.

The first test of this hypothesis is to compare the XW simulation and the YW simulation, which is identical to the XW simulation except that the oscillating winds are oriented across the front (in y) rather than along the front (in x, see Table 1). The comparison focuses on the less dense side of the front, where the increase in depth-integrated biomass over 64 days is largest in both simulations. Although the average vertical diffusivity and viscosity profiles are similar in the XW and YW simulations (Figure 12b), the vertical displacements (within a forcing period and averaged across a forcing period) (Figure 12a), the depth-integrated biomass B_{int} (Figure 13c), and the advective nutrient flux convergence above $z = -120$ m (Figure 13f) are all substantially reduced on the less dense side of the front in the YW simulation compared to the XW simulation. In particular, the amplitude of the oscillatory vertical displacements is reduced from $|\zeta - \langle\zeta\rangle| \sim 10$ m in XW to $|\zeta - \langle\zeta\rangle| \sim 1$ m in YW, and the Lagrangian mean vertical displacement at 64 days is reduced from about $\langle\zeta\rangle \approx 15$ m in XW to $\langle\zeta\rangle \approx 4$ m in YW. The percent increase in B_{int} from 0 to 64 days is reduced from about 50% in XW to 15% in YW, and the advective nutrient flux convergence above $z = -120$ m is reduced from about 2 mmol N/(m^{2}d) in XW to 0.75 mmol N/(m^{2}d) in YW. In fact, the YW simulation is closer to the NF simulation,

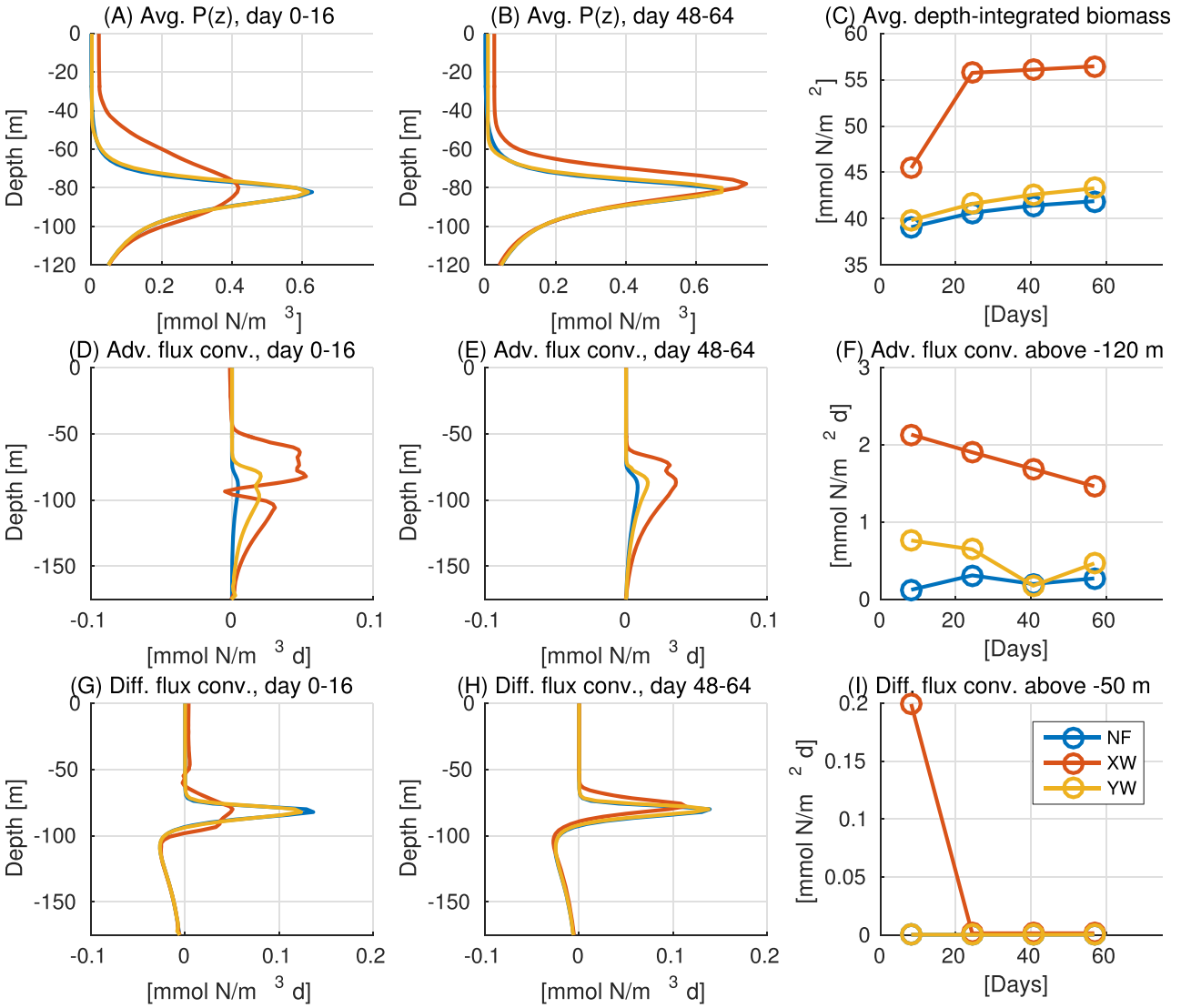

Figure 13. A comparison between three simulations with different imposed forcing parameters, as indicated in the legend in (I): (NF) no wind forcing, (XW) along-front wind stress $\tau_x = .18\cos(.09ft)$, and (YW) cross-front wind stress $\tau_y = .18\cos(.09ft)$. Plots show average vertical profiles of (a and b) phytoplankton $\bar{P}^{y,t}(z)$, (d and e) advective flux convergence $\overline{-\nabla_{y,z} \cdot \mathbf{v}N}^{y,t}$, and (g and h) diffusive flux convergence $\overline{\partial/\partial z(K_z \partial N/\partial z)}^{y,t}$ averaged on the less dense side of the front from $y = 0$ to 15 km and from $t = 0$ to 16 days (a, d, and g) and $t = 48$–64 days (b, e, and h). The right plots show time series of horizontally averaged ($y = 0$–15 km) and (c) full-depth-integrated biomass B_{int}, (f) advective nutrient flux convergence $\overline{\int_{z=-120m}^{0} -\nabla_{y,z} \cdot \mathbf{v}N dz}^{y,t}$, and (i) diffusive nutrient flux convergence $\overline{\int_{z=-50m}^{0} \partial/\partial z(K_z \partial N/\partial z) dz}^{y,t}$, all of which are averaged every 16 days before plotting.

where no wind forcing is applied, than the XW simulation based on these metrics (Figure 13). These results support the hypothesis that the orientation of the wind and the associated Ekman transport are more important for driving the biogeochemical response than the wind-driven variations in the viscosity and diffusivity (in the absence of the explicit oscillatory along-front wind).

Further support for the hypothesis is presented in the supporting information, where the XW and YW simulations are compared with a time-dependent variable mixing (VMT) sensitivity simulation that has the same spatially and temporally variable vertical diffusivity and viscosity as the XW simulation but zero surface wind stress (in the VMT simulation, $K_z(y,z,t)$ and $\nu_z(y,z,t)$ are model inputs derived from the output of the XW simulation rather than from KPP). For the same metrics shown in Figure 13, the VMT simulation is closer to the YW and NF simulations than the XW simulation (see supporting information Figure S10). Hence, although vertical viscosity and diffusivity of density can drive vertical circulations in the front, the vertical viscosity and diffusivity of density are not sufficient by themselves (in the absence of the explicit oscillatory

along-front wind) to induce the advective nutrient flux and phytoplankton response that occurs in the XW scenario.

4.3.1. Discussion

The analysis of sections 4.2–4.3 demonstrates that the enhanced time-mean vertical circulation in the pycnocline is the primary cause of the enhanced biomass at the SPM on the less dense side of the front at late times in the XW simulation. In addition, the analysis rules out some well-known explanations for how winds drive mean vertical circulations and thereby enhance biomass in the SPM at a front. For example, the wind stresses in XW, YW, and NF are chosen so that the time-averaged vertical displacement (over an integer number of forcing periods) due to Ekman suction (defined in (1)) is approximately zero in all cases, so time-mean Ekman suction cannot explain the mean vertical displacements. Moreover, since the biogeochemical response in the NF, YW, and VMT simulations differ from the XW simulation, neither SXL mixing nor interior mixing below the SXL (in the absence of the explicit oscillatory along-front wind stress) can fully explain the enhanced time-mean vertical velocity and the associated enhanced advective nutrient flux (Figures 13d and 13f) and enhanced biomass (Figures 13a–13c) in the XW simulation.

However, the vertical velocity below the SXL in the YW and NF simulations can be explained quantitatively using the theory for a steady frictionally driven vertical circulation,

$$w \approx \frac{\partial}{\partial y}\left(\frac{\nu_z}{f^2}\frac{\partial b}{\partial y}\right), \tag{9}$$

in *Garrett and Loder* [1981]. The 2-D simulations have a nearly constant interior vertical viscosity below the SXL, $\nu_z \approx 2\times10^{-4}$ m^2/s (the turbulent Prandtl number $\nu_z/K_z \approx 10$) [e.g., *Large et al.*, 1994], the horizontal frontal width scale $F_W = 7$ km (see supporting information section S3), and the cross-front buoyancy anomaly scale is $b^* = 8\times10^{-4}$ m/s^2 (see supporting information section S3). Using these values to scale (9) yields an estimate for the mean vertical velocity $\langle w\rangle \approx 0.03$ m/d and the mean vertical displacement $\langle\zeta\rangle \approx 2$ m over 64 days, which is within a factor of two of the Lagrangian mean displacements observed over 64 days in the YW and NF simulations ($\langle\zeta\rangle \lesssim 4$ m) but substantially smaller than the Lagrangian mean vertical displacement observed in the XW simulation ($\langle\zeta\rangle \approx 15$ m) (Figure 12a).

Since the pycnocline is nearly adiabatic in all these simulations (the vertical diffusivity of density is $K_z \approx 2\times10^{-5}$ m^2/s below the boundary layer and the explicit horizontal diffusivity $K_h = 0$ m^2/s; see Figure 12b), Lagrangian fluid parcels essentially maintain their density and the mean Lagrangian vertical circulation in all three simulations is associated with the flattening of frontal isopycnals and a reduction of the horizontal buoyancy gradient in the front (Figures 12c and 12d). If the stratification $N^2 = \partial b/\partial z$ and vertical viscosity ν_z are assumed to vary sufficiently slowly in y, then the time evolution of the horizontal buoyancy gradient is dominated by the differential vertical advection associated with (9), which can be written as a diffusion equation using (9) [*Garrett and Loder*, 1981], that is

$$\frac{\partial}{\partial t}\left(\frac{\partial b}{\partial y}\right) \approx \frac{\nu_z N^2}{f^2}\frac{\partial^2}{\partial y^2}\left(\frac{\partial b}{\partial y}\right). \tag{10}$$

Using the same pycnocline scales in (10) as in (9) implies $\frac{\partial^2 b}{\partial y \partial t} \approx 9\times10^{-16}$ s^{-3}, which is within a factor of two of the values (1.6×10^{-15} s^{-3}) derived from the NF and YW simulations but lower than the value derived from the XW simulation (3×10^{-15} s^{-3}) (Figure 12c). On the other hand, in the highly viscous SXL at the front, where $\nu_z \approx 1$ to 2×10^{-2} m^2/s and $N^2 \approx 1$ to 3×10^{-6} s^{-2} (averaged in time from 0 to 64 days in the XW simulation), the magnitude of the horizontal buoyancy gradient decreases at a similar forcing-period-averaged rate in both the YW and XW simulations. Using representative SXL values for $\nu_z = 0.015$ m^2/s and $N^2 = 1.5\times10^{-6}$ s^{-2} in (10) yields $\frac{\partial^2 b}{\partial y \partial t} \approx 5\times10^{-15}$ s^{-3}, which is essentially the same as the simulated forcing-period-averaged $\frac{\partial^2 b}{\partial y \partial t}$ in the SXL of both the XW and YW simulations (Figure 12d) and significantly faster than the forcing-period-averaged $\frac{\partial^2 b}{\partial y \partial t}$ in the NF simulation where there is no SXL.

In summary, the frictional frontal circulation theory in *Garrett and Loder* [1981] provides several useful scalings for the vertical velocity and frontal spin-down rate in the XW, YW, and NF simulations. Unfortunately, neither the frictional circulation theory in *Garrett and Loder* [1981] nor *any* other frictional circulation theory (which does not explicitly include the effects of the oscillatory wind) can provide an adequate prediction of the faster upwelling velocity (Figure 12a) and faster frontal spin-down rate in the pycnocline (Figure 12c) under XW wind compared to YW wind, which is responsible for the enhanced B_{int} on the less dense side of

the front in the XW simulation (Figure 13c). Some physical mechanisms that may contribute to the more rapid frontal spin-down under oscillatory along-front wind include shear dispersion (i.e., enhanced horizontal mixing) of the density and/or momentum [e.g., *Garrett and Loder*, 1981; *Young et al*., 1982] below the SXL or other nonlinear or asymmetric aspects of the oscillatory secondary circulation in the cross-front plane [e.g., *Thomas and Lee*, 2005]. An analysis of the volume-integrated kinetic and available potential energy budgets in the front centered at $y = 0$ km in the XW, YW, and NF simulations shows that the faster frontal spin-down rate in XW (Figure 13c) is explicitly associated with a more rapid decay of both the kinetic and available potential energy [e.g., *Holliday and Mcintyre*, 1981; *Winters and Barkan*, 2013] associated with the front. In particular, the available potential energy is reduced by 8% over 75 days in the XW simulation compared to 5–6% in the YW and NF simulations. Likewise, the kinetic energy is reduced by 20% over 75 days in the XW simulation compared to 14–15% in the YW and NF simulations (the initial available potential energy is about 3 times the initial kinetic energy). However, a full investigation of the energetics of the frontal spin-down under unsteady wind is beyond the scope of this paper and will be reported elsewhere; this work, which highlights the potential biogeochemical significance of the faster frontal spin-down rate under oscillatory along-front wind, is merely a first step toward that end.

5. Realistic Wind Stress

The results conclude with an analysis of a simulation forced by a realistic wind (RW) scenario (see Table 1), which brings together all wind directions and all resolved frequencies including a time-mean and high-frequency near-inertial winds. But the wind stress is spatially uniform, as in previous sections. The analysis does not explicitly separate the interacting effects of different frequencies in the wind; that analysis is beyond the scope of this paper (but see *Whitt et al*. [2017]). Instead, the RW simulation highlights the robustness of the results developed in previous sections and gives some insight into the relative significance of the synoptic-to-planetary scale wind variability relative to other frequencies. The chosen RW stress time series (plotted in Figure 14a) is derived from summertime measurements of wind speed and direction about 450 km west of Bermuda at the National Data Buoy Center station 41048 using the algorithm of *Large and Pond* [1981]. The front is oriented such that the observed zonal wind points in the along-front (x) direction and the observed meridional wind points in the cross-front (y) direction. The time-mean stress over 64 days is $\tau_x = -.012$ N/m^2 (equivalent to a 2.5 m/s wind at 10 m height), hence the time-integrated stress over 64 days in the RW scenario is approximately the same as the time-integrated stress over 13 days in the CW scenario (although results are only reported out to 8 days in the CW scenario). In addition, the peak wind stress magnitude and wind stress variance in the RW scenario are approximately comparable to the peak wind stress magnitude and wind stress variance in the XW scenario (in section 4).

The results of the RW simulation are consistent with the results of both the CW and XW simulations in that the vertical profiles of biogeochemical variables are essentially unchanged by the wind outside the fronts, but B_{int} is enhanced at the fronts due to enhanced vertical nutrient transport to the euphotic zone there (Figures 14 and 15).

Like the CW simulation, the physical and biogeochemical dynamics in the RW simulation are strongly impacted by the time-integrated along-front wind stress, which drives the time-integrated Ekman buoyancy flux $\int_0^t EBF(s)ds$ and time-integrated Ekman suction $\zeta = \int_0^t w_{Ek}(s)ds$ at the fronts. As a result, snapshots of the phytoplankton distribution after 30 days of down-front RW forcing are qualitatively similar to snapshots of the phytoplankton distributions after 4 (or 8) days of down-front CW forcing (cf., Figure 15c with 2d and supporting information Figure S12d), and likewise for the time-mean up-front forcing (cf., Figure 15d with 2c and supporting information Figure S12c). Due to $\int_0^t EBF(s)ds$, surface mixing layers are deeper, vertical nutrient fluxes are larger, and P_{int} is greater on the less dense side of the fronts forced by time-integrated down-front wind compared to the fronts forced by time-integrated up-front wind (Figure 14). However, the cross-front average P_{int} is enhanced at both fronts due to the tripolar pattern of vertical displacements to the nutricline and SPM driven by Ekman suction (Figure 15), which was discussed in detail in the context of the CW and XW simulations in sections 3 and 4.

Like the XW simulation, deep mixing and entrainment in the RW simulation are intermittent in time and depend strongly on the PV in the pycnocline, not merely the magnitude and direction of the wind. For example, brief periods of relatively-high-amplitude down-front wind, for example on days 9–12, 32–35, and

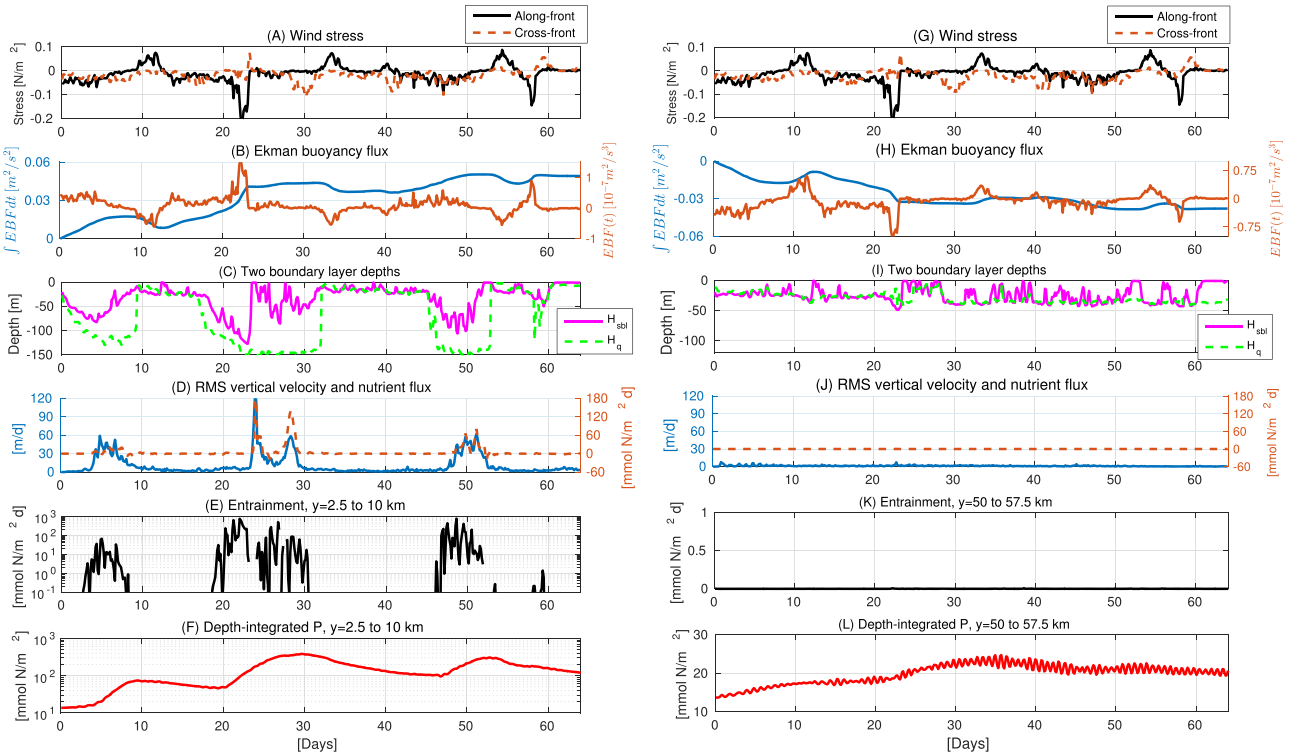

Figure 14. Time series of several variables (calculated exactly as described in Figure 6) for each of the two fronts in the simulation forced by realistic winds (labeled RW in Table 1), where the wind stress is derived from summertime measurements of wind speed and direction at a meteorological station about 450 km west of Bermuda, as described in the text. The left column shows results from the front (centered at $y \approx 0$ km) where the time-mean along-front wind $\overline{\tau_x}^t = -.012$ N/m^2 (averaged over 64 days) is down-front and the time-integrated *EBF* is positive. The right column shows results from the front (centered at $y \approx 60$ km) where the time-mean along-front wind is up-front and the time-integrated *EBF* is negative. Note that the *y*-axes are not the same in both columns here. The phytoplankton distribution $P(y, z)$ at 30 days is shown for the front at $y = 0$ km (the left column here) in Figure 15c and for the front at $y = 60$ km (the right column here) in Figure 15d.

53–56, have little impact on the SXL and induce no nutrient entrainment in the front where the time-mean along-front wind is pointed up-front (Figure 14i). On the other hand, where the time-mean along-front wind is pointed down-front, even a transient wind event with a small down-front component can induce deep mixing, SI, and large upward nutrient fluxes at the front, e.g., between days 24 and 30 in Figures 14a–14e). These results underscore the importance of low PV at the base of the SXL as a preconditioner for deep mixing and entrainment. Although the PV at the SXL base can be modified by many processes in the ocean, these simulations highlight the significance of wind-driven modifications to the PV at the base of the SXL: time-integrated up-front wind is associated with a negative $\int_0^t EBF(s)ds$, which represents a time-integrated source of PV [e.g., *Thomas*, 2005] that concentrates in a sharp pycnocline just below the SXL with high PV and high stratification (Figure 15d). This high-PV layer insulates the nutricline from the effects of intermittent wind events, including down-front wind events, and limits SXL deepening. On the other hand, time-integrated down-front wind is associated with positive $\int_0^t EBF(s)ds$, which represents a time-integrated sink of PV [e.g., *Thomas*, 2005] and preconditions the front for deep mixing. In that case, even a small-amplitude wind event can trigger SI and drive substantial deepening of the SXL (Figure 15c).

6. Conclusions and Discussion

The results of this paper support the well-established hypothesis that winds enhance upwelling and turbulent mixing at ocean fronts and therefore enhance upward nutrient fluxes and phytoplankton biomass in nutrient-limited open oceans. In addition, this paper expands our conceptual understanding of the physical processes that enhance vertical nutrient transport at fronts. The paper makes three main contributions.

First, the largest vertical nutrient fluxes and hence the largest phytoplankton anomalies at fronts occur when anomalously deep mixing layers penetrate the nutricline at fronts. Section 3 presents a new analytic theory for the surface mixing layer depth, which is derived from the flux form of the potential vorticity

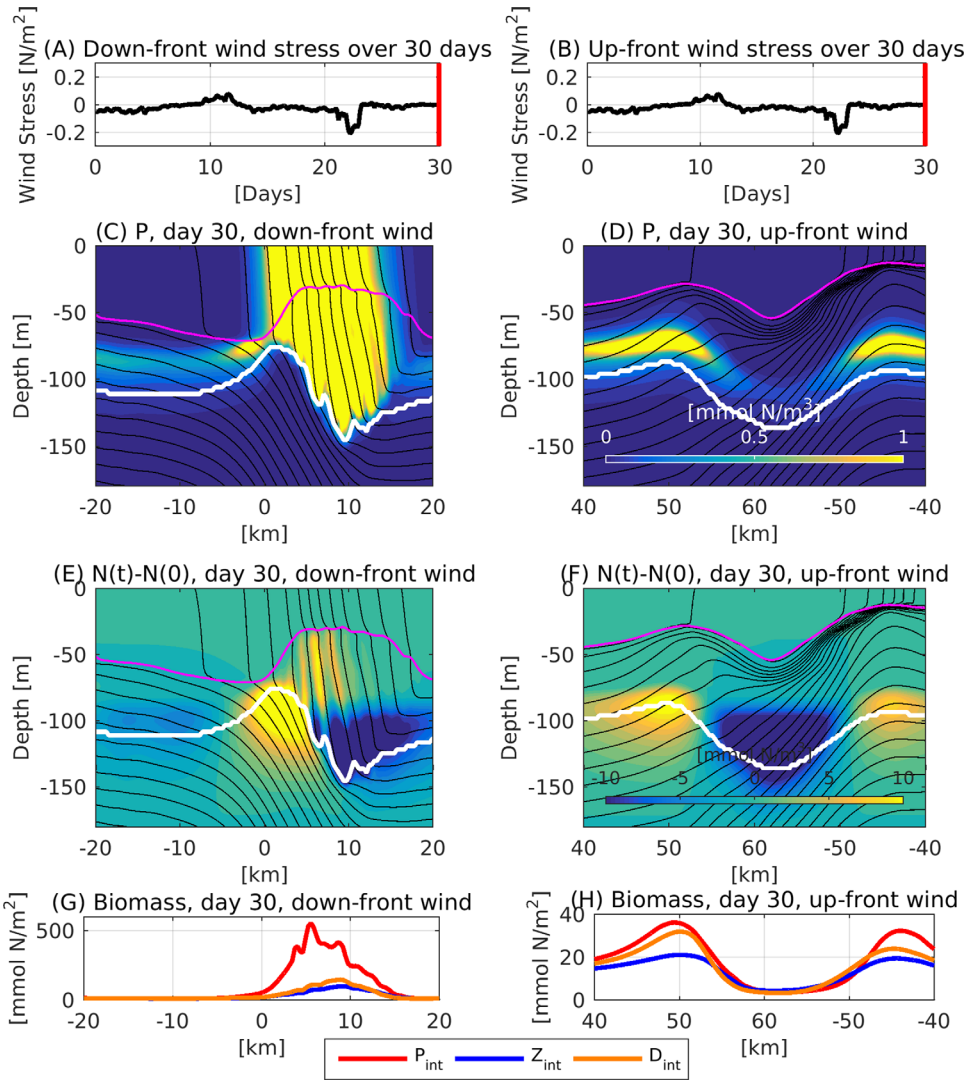

Figure 15. Snapshots of the biogeochemistry on day 30 in the RW scenario. (left) The front centered at $y = 0$ km, where the time-mean wind points down-front, and (right) The front centered at $y = \pm 60$ km, where the time-mean wind points up-front. (a and b) Wind stress time series, (c and d) phytoplankton concentration P, and (e and f) nutrient concentration anomaly, i.e., $N(t=30\ \text{d}) - N(0)$. Overlaid in Figures 15c–15f are density contours every.025 kg/m^3 in black, the depth of the $N = 15$ mmol/m^3 nutrient isopleth $H_{N=15}$ in white, and the high-diffusivity SBL depth H_{sbl} in magenta. (g and h) show full-depth-integrated phytoplankton P_{int} in red, zooplankton Z_{int} in blue, and detritus D_{int} in orange (note the different y axis scales).

equation and includes the effects of symmetric instability on nutrient transport in the surface mixing layer, as in *Taylor and Ferrari* [2010]. The new model adds the effects of variable vertical vorticity and Ekman suction, which significantly deepen the surface mixing layer and enhance entrainment at an isolated front. Therefore, these vertical vorticity effects are necessary to accurately characterize the deepest mixing layers, entrainment, vertical nutrient fluxes, and phytoplankton growth at strong isolated fronts forced by destabilizing down-front wind.

Second, unsteady winds introduce physical and biogeochemical hysteresis (i.e., memory) effects that are not present in process studies of fronts forced by constant winds. Section 4 uses the results of 2-D simulations to highlight two physical hysteresis effects that modify vertical nutrient transport and phytoplankton biomass distributions at a front forced by unsteady wind. First, fronts adjust to oscillatory along-front wind so as to suppress deep mixing and symmetric instability in the SXL, even during periods of destabilizing down-front wind. Second, oscillatory along-front wind speeds the spin-down of the front and enhances the mean vertical circulation in the pycnocline below the SXL. In addition, it is shown: (1) that oscillatory vertical velocities associated with Ekman suction result in transient modifications to the SPM over days to weeks

whereas mean upwelling sustains enhanced phytoplankton at the SPM over weeks to months, and (2) that the mean upwelling cannot be explained by *any* theory for a frictionally driven frontal secondary circulation that does not include an explicit oscillatory along-front stress. However, future work is still necessary to clarify the dynamics and energetics of the frontal spin-down and mean vertical circulation under oscillatory along front wind.

Finally, section 5 presents results from a simulation forced by realistic wind. These simulations emphasize that, in the right circumstances, fronts can be associated with dramatically larger vertical nutrient fluxes to the euphotic zone and much greater depth-integrated phytoplankton biomass than the waters on either side. In addition, the results demonstrate that the vertical nutrient flux and phytoplankton biomass accumulation that result from a synoptic-to-planetary scale wind event at a front depend strongly on the preconditioning of the potential vorticity at the base of the mixed layer, which is modified by the time-integrated Ekman buoyancy flux and hence past wind events. As a result, deep mixing is intermittent in space and time and can be decoupled in time from the wind stress, even in the absence of other sources of physical variability.

These results represent a step toward a more complete understanding of the impact of unsteady synoptic-to-planetary scale wind variability on biogeochemistry at ocean fronts. However, there are several physical and biogeochemical model sensitivities that are relevant to biogeochemistry at a front forced by unsteady wind and have not been explicitly considered in the analysis presented here. For example, it is likely that biogeochemistry at fronts depends on interactions between the wind-driven physical processes discussed here and physical processes that have been excluded here, including resolved upper ocean turbulence [e.g., *Taylor*, 2016], frontal meandering [e.g., *Lévy et al*., 2009], mixed layer baroclinic instabilities [e.g., *Mahadevan et al*., 2010, 2012], small-scale spatial gradients in the wind stress [e.g., *Martin and Richards*, 2001; *McGillicuddy et al*., 2007; *Gaube et al*., 2015], as well as other larger-scale oceanic and atmospheric processes. In addition, the results may be sensitive to the biogeochemical modeling choices, including the spatial structure of the initial condition [e.g., *Franks and Walstad*, 1997], and the biogeochemical model and parameters more generally. Many of these limitations of the present study can be addressed in future modeling experiments. Process studies can be readily devised to isolate and build conceptual understanding of the interactions between particular processes. In addition, larger and more realistic domains are computationally feasible and can be used to explore the aggregated impacts of synoptic-to-planetary scale atmospheric variability on biogeochemistry in an upper ocean with a field of turbulent mesoscale and submesoscale variability. Alternatively, very high-resolution large eddy simulation models can be coupled to the biogeochemistry model in order to explore how resolved upper ocean turbulence modifies the frontal dynamics and biogeochemistry at fronts. Finally, remote and in situ observations of fronts can be used to assess the relationships between unsteady winds and biogeochemistry and to test whether the observations are consistent with existing models (see *Carranza et al*. [2017] for a recent observational study that focuses on the role of synoptic along-front wind variability in modifying surface chlorophyll at a front, similar to this study). In any case, the analysis presented here builds on and supports existing studies that suggest wind-driven vertical transport at fronts, via both turbulent mixing and vertical advection, has a significant impact on biology at fronts in real nutrient-limited open oceans. The results presented here, which focus on the role of unsteady synoptic-to-planetary scale wind variability, emphasize that the biogeochemical impacts of wind forcing may be rather dramatic at fronts, but that the biogeochemical impacts under realistic unsteady wind stresses are expected to be very intermittent in space and time.

Appendix A: Nutrient Entrainment

The nutrient entrainment flux and associated entrainment velocity are defined from the equation for the vertically averaged nutrient concentration in a layer bounded by the surface above and a measure of the surface mixing layer depth $z=H<0$ below, which is not, in general, a material surface (as in *Stevenson and Niiler* [1983]). We present the derivation here. In particular, begin with the nutrient evolution and the continuity equations,

$$\frac{\partial N}{\partial t}=-\frac{\partial vN}{\partial y}-\frac{\partial wN}{\partial z}+\frac{\partial}{\partial z}\left(K_z\frac{\partial N}{\partial z}\right)+\mathcal{R}, \tag{A1}$$

$$\frac{\partial v}{\partial y} = -\frac{\partial w}{\partial z}, \tag{A2}$$

where $\mathcal{R}$ represents all reactive terms (see supporting information section S4 for details). Integrate equations (A1) and (A2) from an arbitrary variable depth $H(x,y,t) < 0$ to $z = 0$ and use the Leibniz rule to obtain:

$$\begin{aligned} -H\frac{\partial \bar{N}}{\partial t} - \frac{\partial H}{\partial t}(\bar{N} - N(H)) = \frac{\partial H}{\partial y}\left(\overline{vN} - v(H)N(H)\right) + H\frac{\partial \overline{vN}}{\partial y} \\ + w(H)N(H) - K_z(H)\frac{\partial N(H)}{\partial z} - H\overline{\mathcal{R}}, \end{aligned} \tag{A3}$$

$$-H\frac{\partial \bar{v}}{\partial y} - \bar{v}\frac{\partial H}{\partial y} + \frac{\partial H}{\partial y}v(H) = w(H), \tag{A4}$$

where the overbar denotes the depth average over the layer bounded by H, for example $\bar{N} = -\frac{1}{H}\int_H^0 N dz$. Then define the perturbation from the depth average (denoted by a prime) such that the integrated perturbation is equal to zero, e.g., $\overline{N'} = 0$ and $N = \bar{N} + N'$, hence $\overline{\bar{N}N'} = 0$ so that (A3) and (A4) can be rewritten as:

$$\begin{aligned} -H\frac{\partial \bar{N}}{\partial t} - H\bar{v}\frac{\partial \bar{N}}{\partial y} = +H\frac{\partial \overline{v'N'}}{\partial y} + \frac{\partial H}{\partial y}\overline{v'N'} \\ + \frac{\partial H}{\partial t}(\bar{N} - N(H)) + H\bar{N}\frac{\partial \bar{v}}{\partial y} \\ + \frac{\partial H}{\partial y}(\bar{v}\bar{N} - v(H)N(H)) \\ + w(H)N(H) - K_z(H)\frac{\partial N(H)}{\partial z} - H\overline{\mathcal{R}}, \end{aligned} \tag{A5}$$

$$0 = H\frac{\partial \bar{v}}{\partial y} + \bar{v}\frac{\partial H}{\partial y} - \frac{\partial H}{\partial y}v(H) + w(H). \tag{A6}$$

Then substitute $w(H)\bar{N} - v(H)\bar{N}\frac{\partial H}{\partial y} = -H\bar{N}\frac{\partial \bar{v}}{\partial y} - \bar{v}\bar{N}\frac{\partial H}{\partial y}$, derived from (A6) into (A5) to obtain:

$$\begin{aligned} -H\frac{\partial \bar{N}}{\partial t} - H\bar{v}\frac{\partial \bar{N}}{\partial y} - \frac{\partial (H\overline{v'N'})}{\partial y} = \\ + \underbrace{\left(\frac{\partial H}{\partial t} + v(H)\frac{\partial H}{\partial y} - w(H)\right)}_{\text{entrainment flux}}(\bar{N} - N(H)) \\ + \underbrace{\mathcal{F}^N_{atm}}_{\text{air/sea flux}} - \underbrace{K_z(H)\frac{\partial N(H)}{\partial z}}_{\text{mixing across base}} - H\overline{\mathcal{R}}, \end{aligned} \tag{A7}$$

which can be rewritten,

$$\begin{aligned} \frac{\partial \bar{N}}{\partial t} + \underbrace{+\bar{v}\frac{\partial \bar{N}}{\partial y}}_{\text{transport by the depth-average flow}} + \underbrace{\frac{\partial \overline{v'N'}}{\partial y}}_{\text{transport by perturbation flow}} = \underbrace{+\frac{w_{en}}{|H|}(\bar{N} - N(H))}_{\text{entrainment}} \\ + \underbrace{\frac{\mathcal{F}^N_{atm}}{|H|}}_{\text{air/sea flux}} - \underbrace{\frac{K_z(H)}{|H|}\frac{\partial N(H)}{\partial z}}_{\text{mixing across base}} + \underbrace{\overline{\mathcal{R}}}_{\text{reaction}}, \end{aligned} \tag{A8}$$

where the *entrainment velocity* is defined to be

$$w_{en} = \frac{\partial H}{\partial t} + v(H)\frac{\partial H}{\partial y} - w(H) = \frac{\partial H}{\partial t} + \frac{\partial (H\bar{v})}{\partial y}, \tag{A9}$$

and the second equality is derived using (A6). In (A9), w_{en} is defined to be positive upwards and negative downwards and indicates the vertical direction of motion of the surface at depth H due to entrainment. For example, we say that the entrainment flux is positive when the time tendency $\partial \bar{N}/\partial t$ associated with

entrainment is positive, that is when $w_{en}(\bar{N}-N(H))$ is positive, which occurs when $N(H) > \bar{N}$ and w_{en} is negative for example. In this paper, we restrict attention to positive entrainment fluxes, that is we consider only

$$\mathcal{F}^{+}_{en}=\mathcal{H}\{w_{en}[\bar{N}-N(H)]\}[w_{en}(\bar{N}-N(H)], \tag{A10}$$

where $\mathcal{H}$ is the Heaviside unit step function defined by $\mathcal{H}(x)=1$ for $x \geq 0$ and $\mathcal{H}=0$ otherwise.

Appendix B: Low PV Layer

The time-evolution equation for the depth $H_{\bar{q}}$ is derived without approximation from the flux form of the PV equation [e.g., *Marshall and Nurser*, 1992; *Thomas*, 2005],

$$\frac{\partial q}{\partial t}=\underbrace{-\frac{\partial vq}{\partial y}-\frac{\partial wq}{\partial z}}_{\text{advection}}-\underbrace{\nabla_{y,z}\cdot\mathcal{F}}_{\text{viscous}}-\underbrace{\nabla_{y,z}\cdot\mathcal{D}}_{\text{diabatic}}, \tag{B1}$$

where $\partial/\partial x=0$ has been assumed, the viscous PV flux divergence $\nabla_{y,z}\cdot\mathcal{F}=\nabla_{y,z}\cdot[f\nabla b\times\mathbf{F}]=\nabla_{y,z}\cdot\left[0, fF_x\frac{\partial b}{\partial z}, -fF_x\frac{\partial b}{\partial y}\right]$ where $\mathbf{F}=D\mathbf{u}_{x,y}/Dt+f(\mathbf{k}\times\mathbf{u}_{x,y})+\nabla_{x,y}p/\rho_0$ and the diabatic PV flux divergence $\nabla_{y,z}\cdot\mathcal{D}=\nabla_{y,z}\cdot\left[-f(f\mathbf{k}+\nabla\times\mathbf{u}_{x,y})B\right]=\nabla_{y,z}\cdot\left[0, -f\frac{\partial u}{\partial z}B, -f(f-\frac{\partial u}{\partial y})B\right]$, $B=Db/Dt$, and the material derivative $D/Dt=\partial/\partial t+v\partial/\partial y+w\partial/\partial z$. We then write an exact evolution equation for the vertically averaged potential vorticity $\bar{q}$ over a surface layer of depth $|H|$ that extends from the surface to $z=H$ (H is defined to be negative, but is otherwise arbitrary at this stage),

$$\begin{aligned}
&-H\frac{\partial\bar{q}}{\partial t}-H\bar{v}\frac{\partial\bar{q}}{\partial y}\\
&+\frac{\partial}{\partial y}\left(\int_H^0 v'q'dz\right)\\
&+(\bar{q}-q(H))\underbrace{\left(-\frac{\partial H}{\partial t}-v(H)\frac{\partial H}{\partial y}+w(H)\right)}_{\text{entrainment velocity}}\\
&=\underbrace{-\mathcal{F}_z|^0_H-\int_H^0\frac{\partial\mathcal{F}_y}{\partial y}dz}_{\text{frictional PV flux}}-\underbrace{\mathcal{D}_z|^0_H-\int_H^0\frac{\partial\mathcal{D}_y}{\partial y}dz}_{\text{diabatic PV flux}},
\end{aligned} \tag{B2}$$

where the primes denote a deviation from the vertical average, which is denoted by an overbar, and the derivation is essentially via the Leibniz rule as in Appendix A. We then *define* $H=H_{\bar{q}}$, whereby the first line of (B2) becomes zero and the entrainment velocity,

$$w^q_{en}=\frac{\partial H_{\bar{q}}}{\partial t}+v(H_{\bar{q}})\frac{\partial H_{\bar{q}}}{\partial y}-w(H_{\bar{q}}), \tag{B3}$$

can be written exactly as

$$w^q_{en}=\frac{1}{q(H_{\bar{q}})}\left(\underbrace{-\mathcal{F}_z|^0_{H_{\bar{q}}}-\int_{H_{\bar{q}}}^0\frac{\partial\mathcal{F}_y}{\partial y}dz}_{\text{frictional PV flux}}\underbrace{-\mathcal{D}_z|^0_{H_{\bar{q}}}-\int_{H_{\bar{q}}}^0\frac{\partial\mathcal{D}_y}{\partial y}dz}_{\text{diabatic PV flux}}\underbrace{-\frac{\partial}{\partial y}\left(\int_{H_{\bar{q}}}^0 v'q'dz\right)}_{\text{instabilities/adjustment}}\right), \tag{B4}$$

where the entrainment velocity w^q_{en} (and entrainment PV flux $-w^q_{en}q(H_{\bar{q}})$) does not depend explicitly upon the transport by the depth-averaged flow (the second term in the first line of (B2)) and only explicitly depends on frictional and diabatic effects (associated primarily with atmospheric forcing) as well as net restratification or destratification induced by resolved small scale instability or adjustment processes in the low PV layer.

It may be noted that the depth $H_{\bar{q}}$ is not equivalent to the definitions given by *Thomas et al.* [2013] and *Bachman et al.* [2017]. In *Thomas et al.* [2013], the low-PV layer is defined to be the deepest depth where the bulk geostrophic Richardson number is equal to one, whereas in *Bachman et al.* [2017], the low-PV layer

is defined to be the deepest depth where the bulk hydrostatic PV is zero assuming zero relative vertical vorticity. The definition proposed by *Thomas et al*. [2013] is equivalent to the definition proposed here in the case that all three of the following conditions are met (and equivalent to the definition of *Bachman et al*. [2017] (their (25)) if conditions 2 and 3 of the following are met):

1. the geostrophic force balance is dominant,
2. the vertical relative vorticity $-\partial u/\partial y$ is equal to zero, and
3. the correlations between the perturbations from the depth-average absolute vorticity and buoyancy gradient above $H_{\bar{q}}$ are equal to zero. This third condition implies depth integrals of products are equivalent to products of depth integrals over the low PV layer.

In any case, the exact evolution equation for $H_{\bar{q}}$ is given by

$$\frac{\partial H_{\bar{q}}}{\partial t} = \underbrace{\frac{\partial M_q}{\partial y}}_{\text{pumping/suction}} + \underbrace{w^q_{en}}_{\text{entrainment}}, \tag{B5}$$

where $M_q = \int_{H_q}^{0} v dz$. In particular, changes in the depth of $H_{\bar{q}}$ are due to convergence/divergence of the cross-front flow in the boundary layer, which induces pumping/suction (i.e., vertical advection) of $H_{\bar{q}}$, and nonconservative entrainment/detrainment of water into/from the boundary layer.

The exact expression for the entrainment velocity w^q_{en} (B4) is complicated, but might be reasonably approximated under a steady down-front wind by

$$w^q_{en} \approx \frac{f^2}{q(H_{\bar{q}})}\left(\frac{EBF}{H_{\bar{q}}}\right), \tag{B6}$$

where

$$EBF = \frac{-\tau_x}{\rho f}\frac{\partial b}{\partial y} \tag{B7}$$

is the Ekman buoyancy flux, that is the classic cross-front Ekman transport $\frac{-\tau_x}{\rho f}$ multiplied by the cross-front buoyancy gradient (as in *Thomas* [2005]; *Taylor and Ferrari* [2010]; *Thomas et al*. [2013]). More explicitly, in going from (B4) to (B6), we have made the following assumptions: (1) that the horizontal advective restratification processes and horizontal frictional/diabatic PV fluxes are small compared to the vertical fluxes, (2) that $H_{\bar{q}}$ extends sufficiently deep into the high-PV layer at the top of the pycnocline that frictional and diabatic PV fluxes are negligible there (hence $\mathcal{D}(0)=0$ and $\mathcal{D}(H_{\bar{q}})=0$ in this case), and (3) that the frictional PV flux is constant across the depth of $H_{\bar{q}}$ and zero below $H_{\bar{q}}$ [such that $\mathcal{F}_z(0) = -\frac{\tau_x}{\rho f H_q}\frac{\partial b}{\partial y}|_{z=0}$ and $\mathcal{F}_z(H_{\bar{q}})=0$].

The interpretation of the entrainment velocity (B6) is aided by making an analogy between entrainment induced by a steady down-front wind via (B6) and entrainment induced by a steady surface heat loss from a convective boundary layer in a stratified ocean without a front. In both cases, the approximate entrainment velocity can be written in a similar mathematical form. In a convective boundary layer forced by air-sea heat loss, the entrainment velocity is $w^q_{en} \approx \frac{f^2}{q(H_{sbl})}\frac{\mathcal{Q}}{H_{sbl}}$ where $q = f^2\frac{\partial b}{\partial z}$ and $\mathcal{Q}$ is the air-sea buoyancy flux (positive upward) [e.g., *Deardorff et al*., 1969], which becomes (B6) after replacing the surface buoyancy flux $\mathcal{Q}$ with the Ekman buoyancy flux *EBF* and replacing the f^2N^2 with the full PV (4) in the denominator. With this analogy in mind, down-front wind (positive *EBF*) reduces the ocean buoyancy content in the front and drives entrainment of pycnocline water into the boundary layer. On the other hand, up-front wind (negative *EBF*) increases the ocean buoyancy content in the front, shoals the surface mixing layer, and drives detrainment of boundary layer water to the pycnocline.

Both isolated frontal jets in Figure 1a are associated with strong cross-front gradients in the absolute vertical vorticity $f-\partial u/\partial y$, which induces divergence and convergence of the generalized cross-front Ekman transport,

$$M_{Ek} = -\frac{\tau_x}{\rho(f-\frac{\partial u}{\partial y})}, \tag{B8}$$

which depends inversely on the absolute vorticity $f-\partial u/\partial y$ (as in *Stern* [1965]; *Niiler* [1969]; *Stern* [1975]), and hence Ekman pumping and suction,

$$w_{Ek} = \frac{\partial M_{Ek}}{\partial y} = -\frac{\tau_x}{\rho_0 (f - \partial u/\partial y)^2} \frac{\partial^2 u}{\partial y^2}, \tag{B9}$$

even when the stress has no gradient across the front $\partial \tau_x / \partial y = 0$, as in all the simulations presented in this paper. Under down-front wind, pumping/downwelling occurs on the flanks of the frontal jet and suction/upwelling occurs in the middle of the jet (see (B9)). Upwelling/suction is reflected in the shallow nutricline and positive nutrient anomaly in the middle of the front and downwelling/pumping is reflected in the deeper nutricline and negative nutrient anomalies on the flanks of the front (Figure 2f). The pattern of Ekman pumping and suction is exactly reversed under up-front wind (the sign is switched in (B9)). Downwelling/pumping occurs in the middle of the front and upwelling/suction occurs on the flanks, which is reflected in both the nutrient and phytoplankton anomalies across the front (Figures 2c, 2e, and 2g).

At a strong front, the depth $H_{\bar{q}}$ is modified significantly by both pumping/suction and entrainment. Pumping/suction and entrainment can be considered simultaneously in the time-evolution equation for $H_{\bar{q}}$ (B5) if the cross-front transport in the boundary layer is approximated as in (B8), that is M_{Ek} replaces $M_{\bar{q}}$ in (B5), and the entrainment velocity w_{en}^{q} is approximated as in (B6). Then (B5) becomes

$$\frac{\partial H_{\bar{q}}}{\partial t} = \underbrace{-\frac{\partial}{\partial y}\left(\frac{\tau_x(t)}{\rho\left(f - \frac{\partial u}{\partial y}\right)}\right)}_{\text{pumping/suction}} \underbrace{- \frac{f^2}{q(H_{\bar{q}})H_{\bar{q}}}\left(\frac{\tau_x(t)}{\rho f}\frac{\partial b}{\partial y}\right)}_{\text{entrainment}}, \tag{B10}$$

which can be integrated to obtain $H_{\bar{q}}(y,t)$ assuming $\partial u/\partial y$, $\partial b/\partial y$, and $q(H_{\bar{q}})$, and the initial $H_{\bar{q}}$ are known and not time-varying. The solution to the nonlinear ordinary differential equation (B10) can be written in closed form in terms of a Lambert $\mathcal{W}$ function [*Corless et al.*, 1996] or integrated numerically.

Acknowledgments

Code and output files for the 1-D simulations are archived online [see *Whitt*, 2017a], and output files from the 2-D simulations are archived online [see *Whitt*, 2017b]. DBW was supported by the National Science Foundation postdoctoral research fellowship program, award number 1421125. J.R.T. was supported by the Natural Environment Research Council, award NE/J010472/1. The simulations and analysis were performed in part using computing resources provided by the Department of Applied Mathematics and Theoretical Physics at the University of Cambridge. Finally, the constructive suggestions from two anonymous reviewers are gratefully acknowledged.

References

Abramowitz, M., and I. A. Stegun (Eds.) (1964), *Handbook of Mathematical Functions*, 1046 pp., Dover, New York.

Allen, J. T., et al. (2005), Diatom carbon export enhanced by silicate upwelling in the northeast Atlantic, *Nature*, *437*(7059), 728–732.

Andrews, D. G., and M. E. McIntyre (1978), An exact theory of nonlinear waves on a Lagrangian-mean flow, *J. Fluid Mech.*, *89*(4), 609–646.

Bachman, S. D., and J. Taylor (2014), Modelling of partially-resolved oceanic symmetric instability, *Ocean Modell.*, *82*, 15–27.

Bachman, S. D., B. Fox-Kemper, J. R. Taylor, and L. N. Thomas (2017), Parameterization of frontal symmetric instabilities: I: Theory for resolved fronts, *Ocean Modell.*, *109*, 72–95, doi:10.1016/j.ocemod.2016.12.003.

Beckmann, A., and I. Hense (2007), Beneath the surface: Characteristics of oceanic ecosystems under weak mixing conditions: A theoretical investigation, *Prog. Oceanogr.*, *75*(4), 771–796.

Belkin, I. M., P. C. Cornillon, and K. Sherman (2009), Fronts in large marine ecosystems, *Prog. Oceanogr.*, *81*(1), 223–236.

Brannigan, L. (2016), Intense submesoscale upwelling in anticyclonic eddies, *Geophys. Res. Lett.*, *43*, 3360–3369, doi:10.1002/2016GL067926.

Carranza, M., S. Gille, A. Piola, M. Charo, and S. Romero (2017), Wind modulation of upwelling at the shelf-break front off Patagonia: Observational evidence, *J. Geophys. Res. Oceans*, *122*, 2401–2421, doi:10.1002/2016JC012059.

Claustre, H., P. Kerhervé, J. C. Marty, L. Prieur, C. Videau, and J.-H. Hecq (1994), Phytoplankton dynamics associated with a geostrophic front: Ecological and biogeochemical implications, *J. Mar. Res.*, *52*(4), 711–742.

Corless, R. M., G. H. Gonnet, D. E. Hare, D. J. Jeffrey, and D. E. Knuth (1996), On the Lambert W function, *Adv. Comput. Math.*, *5*(1), 329–359.

Cullen, J. J. (2015), Subsurface chlorophyll maximum layers: Enduring enigma or mystery solved?, *Annu. Rev. Mar. Sci.*, *7*, 207–239.

Davis, R. E., M. D. Ohman, D. L. Rudnick, and J. T. Sherman (2008), Glider surveillance of physics and biology in the southern California Current System, *Limnol. Oceanogr.*, *53*, 2151–2168.

Deardorff, J., G. Willis, and D. K. Lilly (1969), Laboratory investigation of non-steady penetrative convection, *J. Fluid Mech.*, *35*(1), 7–31.

Denman, K. L., and M. R. Abbott (1994), Time scales of pattern evolution from cross-spectrum analysis of advanced very high resolution radiometer and coastal zone color scanner imagery, *J. Geophys. Res.*, *99*(C4), 7433–7442, doi:10.1029/93JC02149.

Edwards, A. M., and J. Brindley (1999), Zooplankton mortality and the dynamical behaviour of plankton population models, *Bull. Math. Biol.*, *61*(2), 303–339.

Edwards, A. M., and A. Yool (2000), The role of higher predation in plankton population models, *J. Plankton Res.*, *22*(6), 1085–1112.

Eliassen, A. (1951), Slow thermally or frictionally controlled meridional circulation in a circular vortex, *Astrophys. Norvegica*, *5*, 19–60.

Fasham, M. J., H. Ducklow, and S. McKelvie (1990), A nitrogen-based model of plankton dynamics in the oceanic mixed layer, *J. Mar. Res.*, *48*(3), 591–639.

Fedorov, K. N. (1986), *The Physical Nature and Structure of Ocean Fronts*, Springer, New York.

Fernández, E., and R. D. Pingree (1996), Coupling between physical and biological fields in the North Atlantic subtropical front southeast of the Azores, *Deep Sea Res. Part I*, *43*(9), 1369–1393.

Ferrari, R. (2011), A frontal challenge for climate models, *Science*, *332*, 316–317.

Franks, P., and L. Walstad (1997), Phytoplankton patches at fronts: A model of formation and response to wind events, *J. Mar. Res.*, *55*(1), 1–29.

Franks, P., J. Wroblewski, and G. Flierl (1986), Behavior of a simple plankton model with food-level acclimation by herbivores, *Mar. Biol.*, *91*(1), 121–129.

Garrett, C., and J. Loder (1981), Dynamical aspects of shallow sea fronts, *Philos. Trans. R. Soc. London A*, *302*(1472), 563–581.

Gaube, P., D. B. Chelton, R. M. Samelson, M. G. Schlax, and L. W. O'Neill (2015), Satellite observations of mesoscale eddy-induced Ekman pumping, *J. Phys. Oceanogr.*, *45*(1), 104–132.
Gill, A. E. (1982), *Atmosphere-Ocean Dynamics*, Academic, London.
Gille, S. T. (2005), Statistical characterization of zonal and meridional ocean wind stress, *J. Atmos. Oceanic Technol.*, (9), 1353–1372.
Gower, J., K. Denman, and R. Holyer (1980), Phytoplankton patchiness indicates the fluctuation spectrum of mesoscale oceanic structure, *Nature*, *288*(5787), 157–159.
Granata, T., J. Wiggert, and T. Dickey (1995), Trapped, near-inertial waves and enhanced chlorophyll distributions, *J. Geophys. Res.*, *100*(C10), 20,793–20,804.
Hamming, R. (1973), *Numerical Methods for Scientists and Engineers*, McGraw-Hill, New York.
Holliday, D., and M. E. Mcintyre (1981), On potential energy density in an incompressible, stratified fluid, *J. Fluid Mech.*, *107*, 221–225.
Holloway, G. (1984), Effects of velocity fluctuations on vertical distributions of phytoplankton, *J. Mar. Res.*, *42*(3), 559–571.
Hoskins, B. (1974), The role of potential vorticity in symmetric stability and instability, *Q. J. R. Meteorol. Soc.*, *100*, 480–482.
Inoue, R., M. C. Gregg, and R. R. Harcourt (2010), Mixing rates across the Gulf Stream, Part 1: On the formation of Eighteen Degree Water, *J. Mar. Res.*, *68*, 643–671.
Klein, P., and G. Lapeyre (2009), The oceanic vertical pump induced by mesoscale and submesoscale turbulence, *Annu. Rev. Mar. Sci.*, *1*, 351–375.
Krause, J. W., M. A. Brzezinski, R. Goericke, M. R. Landry, M. D. Ohman, M. R. Stukel, and A. G. Taylor (2015), Variability in diatom contributions to biomass, organic matter production and export across a frontal gradient in the California Current Ecosystem, *J. Geophys. Res. Oceans*, *120*, 1032–1047, doi:10.1002/2014JC010472.
Large, W. G., and S. Pond (1981), Open ocean momentum flux measurements in moderate to strong winds, *J. Phys. Oceanogr.*, *11*(3), 324–336.
Large, W. G., J. C. McWilliams, and S. C. Doney (1994), Oceanic vertical mixing: A review and a model with a nonlocal boundary layer parameterization, *Rev. Geophys.*, *32*(4), 363–403.
Lee, D.-K., P. Niiler, A. Warn-Varnas, and S. Piacsek (1994), Wind-driven secondary circulation in ocean mesoscale, *J. Mar. Res.*, *52*(3), 371–396.
Lévy, M., and P. Klein (2004), Does the low frequency variability of mesoscale dynamics explain a part of the phytoplankton and zooplankton spectral variability?, *Proc. R. Soc. London Ser. A*, *460*, 1673–1687.
Lévy, M., P. Klein, and A.-M. Treguier (2001), Impact of sub-mesoscale physics on production and subduction of phytoplankton in an oligotrophic regime, *J. Mar. Res.*, *59*(4), 535–565.
Lévy, M., P. Klein, and M. Ben Jelloul (2009), New production stimulated by high-frequency winds in a turbulent mesoscale eddy field, *Geophys. Res. Lett.*, *36*, L16603, doi:10.1029/2009GL039490.
Lévy, M., D. Iovino, L. Resplandy, P. Klein, G. Madec, A.-M. Tréguier, S. Masson, and K. Takahashi (2012a), Large-scale impacts of submesoscale dynamics on phytoplankton: Local and remote effects, *Ocean Modell.*, *43*, 77–93.
Lévy, M., R. Ferrari, P. J. Franks, A. P. Martin, and P. Rivière (2012b), Bringing physics to life at the submesoscale, *Geophys. Res. Lett.*, *39*, L14602, doi:10.1029/2012GL052756.
Li, Q. P., P. J. Franks, M. D. Ohman, and M. R. Landry (2012), Enhanced nitrate fluxes and biological processes at a frontal zone in the southern California Current System, *J. Plankton Res.*, *34*(9), 790–801, doi:10.1093/plankt/fbs006.
Lima, I. D., D. B. Olson, and S. C. Doney (2002), Biological response to frontal dynamics and mesoscale variability in oligotrophic environments: Biological production and community structure, *J. Geophys. Res.*, *107*(C8), 3111, doi:10.1029/2000JC000393.
Mahadevan, A. (2016), The impact of submesoscale physics on primary productivity of plankton, *Annu. Rev. Mar. Sci.*, *8*, 161–184.
Mahadevan, A., and D. Archer (2000), Modeling the impact of fronts and mesoscale circulation on the nutrient supply and biogeochemistry of the upper ocean, *J. Geophys. Res.*, *105*(C1), 1209–1225.
Mahadevan, A., L. N. Thomas, and A. Tandon (2008), Comment on "Eddy/Wind interactions stimulate extraordinary mid-ocean plankton blooms", *Science*, *320*(5875), 448–448.
Mahadevan, A., A. Tandon, and R. Ferrari (2010), Rapid changes in mixed layer stratification driven by submesoscale instabilities and winds, *J. Geophys. Res.*, *115*, C03017, doi:10.1029/2008JC005203.
Mahadevan, A., E. D'Asaro, C. Lee, and M. J. Perry (2012), Eddy-driven stratification initiates north Atlantic spring phytoplankton blooms, *Science*, *337*(6090), 54–58.
Marshall, J. C., and A. G. Nurser (1992), Fluid dynamics of oceanic thermocline ventilation, *J. Phys. Oceanogr.*, *22*(6), 583–595.
Martin, A. P., and K. J. Richards (2001), Mechanisms for vertical nutrient transport within a North Atlantic mesoscale eddy, *Deep Sea Res., Part II*, *48*(4), 757–773.
Martin, A. P., K. J. Richards, and M. J. Fasham (2001), Phytoplankton production and community structure in an unstable frontal region, *J. Mar. Syst.*, *28*(1), 65–89.
McGillicuddy, D. J. (2016), Mechanisms of physical-biological-biogeochemical interaction at the oceanic mesoscale, *Annu. Rev. Mar. Sci.*, *8*, 125–159.
McGillicuddy, D. J., L. Anderson, S. Doney, and M. Maltrud (2003), Eddy-driven sources and sinks of nutrients in the upper ocean: Results from a 0.1° resolution model of the North Atlantic, *Global Biogeochem. Cycles*, *17*(2), 1035, doi:10.1029/2002GB001987.
McGillicuddy, D. J., et al. (2007), Eddy/wind interactions stimulate extraordinary mid-ocean plankton blooms, *Science*, *316*(5827), 1021–1026.
McWilliams, J. C. (2016), Submesoscale currents in the ocean, *Proc. R. Soc. A*, *472*(2189), doi:10.1098/rspa.2016.0117.
McWilliams, J. C., J. Gula, M. J. Molemaker, L. Renault, and A. F. Shchepetkin (2015), Filament frontogenesis by boundary layer turbulence, *J. Phys. Oceanogr.*, *45*(8), 1988–2005.
Mied, R. P., C. Y. Shen, C. L. Trump, and G. J. Lindemann (1986), Internal-inertial waves in a Sargasso Sea front, *J. Phys. Oceanogr.*, *16*(11), 1751–1762.
Moses, W. J., S. G. Ackleson, J. W. Hair, C. A. Hostetler, and W. D. Miller (2016), Spatial scales of optical variability in the coastal ocean: Implications for remote sensing and in situ sampling, *J. Geophys. Res. Oceans*, *121*, 4194–4208, doi:10.1002/2016JC011767.
Nagai, T., A. Tandon, and D. Rudnick (2006), Two-dimensional ageostrophic secondary circulation at ocean fronts due to vertical mixing and large-scale deformation, *J. Geophys. Res.*, *111*, C09038, doi:10.1029/2005JC002964.
Nagai, T., A. Tandon, N. Gruber, and J. C. McWilliams (2008), Biological and physical impacts of ageostrophic frontal circulations driven by confluent flow and vertical mixing, *Dyn. Atmos. Oceans*, *45*(3), 229–251.
Nagai, T., A. Tandon, H. Yamazaki, and M. J. Doubell (2009), Evidence of enhanced turbulent dissipation in the frontogenetic Kuroshio front thermocline, *Geophys. Res. Lett.*, *36*, L12609, doi:10.1029/2009GL038832.

Niewiadomska, K., H. Claustre, L. Prieur, and F. d'Ortenzio (2008), Submesoscale physical-biogeochemical coupling across the Ligurian current (northwestern Mediterranean) using a bio-optical glider, *Limnol. Oceanogr.*, *53*, 2210–2225.
Niiler, P. P. (1969), On the Ekman divergence in an oceanic jet, *J. Geophys. Res.*, *74*(28), 7048–7052.
Omand, M. M., E. A. D'Asaro, C. M. Lee, M. J. Perry, N. Briggs, I. Cetinić, and A. Mahadevan (2015), Eddy-driven subduction exports particulate organic carbon from the spring bloom, *Science*, *348*(6231), 222–225.
Orsi, A. H., T. Whitworth, and W. D. Nowlin (1995), On the meridional extent and fronts of the Antarctic Circumpolar Current, *Deep Sea Res., Part I*, *42*(5), 641–673.
Oschlies, A. (2002), Can eddies make ocean deserts bloom?, *Global Biogeochem. Cycles*, *16*(4), 1106, doi:10.1029/2001GB001830.
Plumb, R. (1979), Eddy fluxes of conserved quantities by small-amplitude waves, *J. Atmos. Sci.*, *36*(9), 1699–1704.
Pollard, R. T., and L. A. Regier (1992), Vorticity and vertical circulation at an ocean front, *J. Phys. Oceanogr.*, *22*(6), 609–625.
Pollard, R. T., P. B. Rhines, and R. Thompson (1972), The deepening of the wind-mixed layer, *Geophys. Astrophys. Fluid Dyn.*, *4*(1), 381–404.
Powell, T. M., C. V. Lewis, E. N. Curchitser, D. B. Haidvogel, A. J. Hermann, and E. L. Dobbins (2006), Results from a three-dimensional, nested biological-physical model of the California Current System and comparisons with statistics from satellite imagery, *J. Geophys. Res.*, *111*, C07018, doi:10.1029/2004JC002506.
Riley, G. A., H. M. Stommel, and D. F. Bumpus (1949), Quantitative ecology of the plankton of the western North Atlantic, *Bull. Bingham Oceanogr. Collect., Yale Univ.*, *12*(3), 1–169.
Rudnick, D., and J. Luyten (1996), Intensive surveys of the Azores front 1. Tracers and dynamics, *J. Geophys. Res.*, *101*(C1), 923–939.
Shchepetkin, A. F., and J. C. McWilliams (2005), The regional ocean modeling system (ROMS): A split-explicit, free-surface, topography-following coordinate oceanic model, *Ocean Modell.*, *9*, 347–404.
Siedlecki, S. A., D. Archer, and A. Mahadevan (2011), Nutrient exchange and ventilation of benthic gases across the continental shelf break, *J. Geophys. Res.*, *116*, C06023, doi:10.1029/2010JC006365.
Siedlecki, S. A., A. Mahadevan, and D. Archer (2012), Mechanism for export of sediment-derived iron in an upwelling regime, *Geophys. Res. Lett.*, *39*, L03601, doi:10.1029/2011GL050366.
Smolarkiewicz, P. K., and L. G. Margolin (1998), MPDATA: A finite-difference solver for geophysical flows, *J. Comput. Phys.*, *140*(2), 459–480.
Steele, J. H., and E. W. Henderson (1992), The role of predation in plankton models, *J. Plankton Res.*, *14*(1), 157–172.
Stern, M. E. (1975), *Ocean Circulation Physics*, Academic, New York.
Stern, M. E. (1965), Interaction of a uniform wind stress with a geostrophic vortex, *Deep Sea Res., Oceanogr. Abstr.*, *12*, 355–367.
Stevenson, J. W., and P. P. Niiler (1983), Upper ocean heat budget during the Hawaii-to-Tahiti shuttle experiment, *J. Phys. Oceanogr.*, *13*(10), 1894–1907.
Straneo, F., M. Kawase, and S. C. Riser (2002), Idealized models of slantwise convection in a baroclinic flow, *J. Phys. Oceanogr.*, *32*(2), 558–572.
Strass, V. H. (1992), Chlorophyll patchiness caused by mesoscale upwelling at fronts, *Deep Sea Res. Part A*, *39*(1), 75–96.
Stukel, M. R., et al. (2017), Mesoscale ocean fronts enhance carbon export due to gravitational sinking and subduction, *Proc. Natl. Acad. Sci.*, *114*(6), 1252–1257.
Taylor, A. G., R. Goericke, M. R. Landry, K. E. Selph, D. A. Wick, and M. J. Roadman (2012), Sharp gradients in phytoplankton community structure across a frontal zone in the California Current Ecosystem, *J. Plankton Res.*, *34*(9), 778–789.
Taylor, J. R. (2016), Turbulent mixing, restratification, and phytoplankton growth at a submesoscale eddy, *Geophys. Res. Lett.*, *43*, 5784–5792, doi:10.1002/2016GL069106.
Taylor, J. R., and R. Ferrari (2010), Buoyancy and wind-driven convection at mixed layer density fronts, *J. Phys. Oceanogr.*, *40*(6), 1222–1242.
Thomas, L. N. (2005), Destruction of potential vorticity by winds, *J. Phys. Oceanogr.*, *35*(12), 2457–2466.
Thomas, L. N., and R. Ferrari (2008), Friction, frontogenesis, and the stratification of the surface mixed layer, *J. Phys. Oceanogr.*, *38*(11), 2501–2518.
Thomas, L. N., and C. Lee (2005), Intensification of ocean fronts by down-front winds, *J. Phys. Oceanogr.*, *35*, 1086–1102.
Thomas, L. N., A. Tandon, and A. Mahadevan (2008), Submesoscale processes and dynamics, in *Ocean Modeling in an Eddying Regime, Geophys. Monogr. Ser.*, *177*, edited by M. W. Hecht and H. Hasumi, pp. 17–37, AGU, Washington, D. C.
Thomas, L. N., J. Taylor, R. Ferrari, and T. Joyce (2013), Symmetric instability in the Gulf Stream., *Deep Sea Res., Part II*, *91*, 96–110.
Thomas, L. N., J. R. Taylor, E. A. D'Asaro, C. M. Lee, J. M. Klymak, and A. Shcherbina (2016), Symmetric instability, inertial oscillations, and turbulence at the Gulf Stream front, *J. Phys. Oceanogr.*, *46*, 197–217.
Thompson, A. F., A. Lazar, C. Buckingham, A. C. Naveira Garabato, G. M. Damerell, and K. J. Heywood (2016), Open-ocean submesoscale motions: A full seasonal cycle of mixed layer instabilities from gliders, *J. Phys. Oceanogr.*, *46*(4), 1285–1307.
Thompson, L. (2000), Ekman layers and two-dimensional frontogenesis in the upper ocean, *J. Geophys. Res.*, *105*(C3), 6437–6451.
Thyssen, M., N. Garcia, and M. Denis (2009), Submesoscale phytoplankton distribution in the North East Atlantic surface waters determined with an automated flow cytometer, *Biogeosciences*, *6*(4), 569–583.
van Gennip, S., A. P. Martin, M. A. Srokosz, J. T. Allen, R. Pidcock, S. C. Painter, and M. C. Stinchcombe (2016), Plankton patchiness investigated using simultaneous nitrate and chlorophyll observations, *J. Geophys. Res. Oceans*, *121*, 4149–4156, doi:10.1002/2016JC011789.
Washburn, L., B. M. Emery, B. H. Jones, and D. G. Ondercin (1998), Eddy stirring and phytoplankton patchiness in the subarctic North Atlantic in late summer, *Deep Sea Res. Part I*, *45*(9), 1411–1439.
Whitt, D. B. (2017a), *A One-Dimensional NPZD Model in Matlab*, v1.0, doi:10.5281/zenodo.569312.
Whitt, D. B. (2017b), Simulation output for "Synoptic-to-planetary scale wind variability enhances phytoplankton biomass at fronts", doi: 10.6084/m9.figshare.c.3768473.v1.
Whitt, D. B., M. Lévy, and J. R. Taylor (2017), Low-frequency and high-frequency oscillatory winds synergistically enhance nutrient entrainment and phytoplankton at fronts, *J. Geophys. Res. Oceans*, *112*, 116–141, doi:10.1002/2016JC012400.
Winters, K. B., and R. Barkan (2013), Available potential energy density for Boussinesq fluid flow, *J. Fluid Mech.*, *714*, 476–488.
Woods, J. (1988), Mesoscale upwelling and primary production, in *Toward A Theory on Biological-Physical Interactions in the World Ocean*, edited by B. J. Rothschild, pp. 7–38, Kluwer Acad. Publ., Boston.
Yoder, J. A., J. Aiken, R. N. Swift, F. E. Hoge, and P. M. Stegmann (1993), Spatial variability in near-surface chlorophyll a fluorescence measured by the Airborne Oceanographic Lidar (AOL), *Deep Sea Res., Part II*, *40*(1–2), 37–53.
Young, W. R., P. B. Rhines, and C. J. R. Garrett (1982), Shear-flow dispersion, internal waves and horizontal mixing in the ocean., *J. Phys. Oceanogr.*, *12*, 515–527.